



**HAL**  
open science

## Dark spots and cold jets in the polar regions of Mars: new clues from a thermal model of surface CO ice

C. Pilorget, F. Forget, E. Millour, M. Vincendon, J.B. Madeleine

### ► To cite this version:

C. Pilorget, F. Forget, E. Millour, M. Vincendon, J.B. Madeleine. Dark spots and cold jets in the polar regions of Mars: new clues from a thermal model of surface CO ice. *Icarus*, 2011, 10.1016/j.icarus.2011.01.031 . hal-00743841

**HAL Id: hal-00743841**

**<https://hal.science/hal-00743841>**

Submitted on 21 Oct 2012

**HAL** is a multi-disciplinary open access archive for the deposit and dissemination of scientific research documents, whether they are published or not. The documents may come from teaching and research institutions in France or abroad, or from public or private research centers.

L'archive ouverte pluridisciplinaire **HAL**, est destinée au dépôt et à la diffusion de documents scientifiques de niveau recherche, publiés ou non, émanant des établissements d'enseignement et de recherche français ou étrangers, des laboratoires publics ou privés.

## Accepted Manuscript

Dark spots and cold jets in the polar regions of Mars: new clues from a thermal model of surface CO<sub>2</sub> ice

C. Pilorget, F. Forget, E. Millour, M. Vincendon, J.B. Madeleine

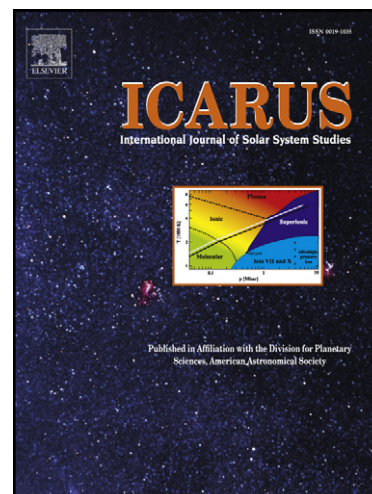
PII: S0019-1035(11)00042-X  
DOI: [10.1016/j.icarus.2011.01.031](https://doi.org/10.1016/j.icarus.2011.01.031)  
Reference: YICAR 9710

To appear in: *Icarus*

Received Date: 5 June 2010  
Revised Date: 18 January 2011  
Accepted Date: 18 January 2011

Please cite this article as: Pilorget, C., Forget, F., Millour, E., Vincendon, M., Madeleine, J.B., Dark spots and cold jets in the polar regions of Mars: new clues from a thermal model of surface CO<sub>2</sub> ice, *Icarus* (2011), doi: [10.1016/j.icarus.2011.01.031](https://doi.org/10.1016/j.icarus.2011.01.031)

This is a PDF file of an unedited manuscript that has been accepted for publication. As a service to our customers we are providing this early version of the manuscript. The manuscript will undergo copyediting, typesetting, and review of the resulting proof before it is published in its final form. Please note that during the production process errors may be discovered which could affect the content, and all legal disclaimers that apply to the journal pertain.



1 Dark spots and cold jets in the polar regions of Mars: new  
2 clues from a thermal model of surface CO<sub>2</sub> ice ☆

3 C. Pilorget<sup>a,1,\*</sup>, F. Forget<sup>a</sup>, E. Millour<sup>a</sup>, M. Vincendon<sup>b</sup>, J.B. Madeleine<sup>a</sup>

4 <sup>a</sup>*Laboratoire de Météorologie Dynamique, CNRS/UPMC/IPSL, 4 place Jussieu, BP99, 75252 Paris*  
5 *Cedex 05, France*

6 <sup>b</sup>*Department of Geological Sciences, Brown University, Providence, RI 02912, USA*

---

7 **Abstract**

Observations of the Martian CO<sub>2</sub> ice cap in late winter and spring have revealed exotic phenomena. Unusual dark spots, fans and blotches form as the south-polar seasonal CO<sub>2</sub> ice cap retreats. The formation mechanisms of these features are not clearly understood. Theoretical models suggest that photons could penetrate deep into the CO<sub>2</sub> ice down to the regolith, leading to basal sublimation and gas and dust ejection. We have developed a detailed thermal model able to simulate the temporal evolution of the regolith-CO<sub>2</sub> ice layer-atmosphere column. It takes into account heat conduction, radiative transfer within the ice and the atmosphere, and latent heat exchange when there is a phase transition. We found that a specific algorithm, fully coupling these 3 components, was needed to properly predict ice sublimation below the surface. Our model allows us to determine under what conditions basal sublimation is possible and thus when and where it can occur on Mars. Our results show that basal sublimation is possible if we consider large pathlengths and very little dust content within the ice. Moreover, the model can explain how dark spots can appear very early after the end of the polar night at high latitudes. We also evaluate the importance of the different parameters in our simulations. Contrary to what was suggested by theoretical models, the role of seasonal thermal waves is found to be limited. Solar radiation alone can initiate basal sublimation, which therefore only depends on the CO<sub>2</sub> ice properties. Three main modes were identified: one where condensation/sublimation only occurs at the surface (in the case of small grains and/or high dust content), one where basal sublimation is possible (large pathlengths and very little dust content) and an intermediate mode where sublimation within the ice may occur. We suggest that these different modes could be keys to understanding

many processes that occur at the surface of Mars, like the anticyclonic area behavior or the recent reported activity in gullies.

- 8 *Keywords:* Mars, polar caps, climate, ices
- 

ACCEPTED MANUSCRIPT

---

<sup>\*</sup>A proposed running head: Modeling Mars polar cold jets in CO<sub>2</sub> ice

<sup>\*</sup>Corresponding author. Tel.: +33 1 69 85 87 32. E-mail address: Cedric.Pilorget@lmd.jussieu.fr

*Email addresses:* Cedric.Pilorget@lmd.jussieu.fr (C. Pilorget),  
Francois.Forget@lmd.jussieu.fr (F. Forget), Ehouarn.Millour@lmd.jussieu.fr (E. Millour),  
Mathieu\_Vincendon@brown.edu (M. Vincendon), Jean-Baptiste.Madeleine@lmd.jussieu.fr  
(J.B. Madeleine)

<sup>1</sup>now at Institut d'Astrophysique Spatiale, Universite de Paris Sud 11, 91405 Orsay, France

## 9 1. Introduction

10 On Mars, about one third of the atmosphere (composed of 95% CO<sub>2</sub>) condenses dur-  
11 ing fall and winter to form polar caps. Because of pressure and temperature conditions  
12 at the surface, there is no CO<sub>2</sub> liquid phase and solid CO<sub>2</sub> directly condenses and sub-  
13 limates. During spring, the insolation increases and the seasonal polar cap disappears  
14 gradually (except in the southern very high latitudes where a small perennial polar cap  
15 remains). The Thermal Emission Spectrometer (TES) onboard the Mars Global Sur-  
16 veyor (MGS) spacecraft has characterized the recession date as defined by the “crocus  
17 date” and the thermal and visual properties of the seasonal polar caps (Kieffer *et al.*  
18 2000; Kieffer and Titus 2001). The Observatoire pour la Mineralogie, l’Eau, les Glaces,  
19 et l’Activite (OMEGA) onboard Mars Express has acquired repeated spectral data of  
20 the polar ices and dust in the visible and near infrared and mapped their distribution  
21 (Bibring *et al.* 2004; Langevin *et al.* 2006; Langevin *et al.* 2007). The MGS Mars Or-  
22 biter Camera (MOC) and Mars Reconnaissance Orbiter (MRO) High Resolution Imaging  
23 Science Experiment (HiRISE) have returned high-resolution images of the polar regions  
24 revealing numerous exotic features. During seasonal polar cap recession, dark spots and  
25 fans appear on the surface. Many of the features look like exposures of subfrost soil,  
26 and have been interpreted as such (Malin and Edgett 2000; Supulver *et al.* 2001), but  
27 the Thermal Emission Imaging System (THEMIS) observations showed that they remain  
28 near the temperatures expected for solid CO<sub>2</sub> for days to months, and therefore must be  
29 in intimate contact with, or composed of, solid CO<sub>2</sub> (Kieffer *et al.* 2006). A proposed  
30 explanation is that solar radiation penetrates into the CO<sub>2</sub> slab, heats the regolith and  
31 sublimates the base of the CO<sub>2</sub> slab, which then levitates above the ground by gas pres-  
32 sure. Gas tries to escape, and when a path to the surface is created, CO<sub>2</sub> gas and dust  
33 are ejected and form these dark spots (Piqueux *et al.* 2003; Kieffer 2007; Portyankina  
34 *et al.* 2010). This process results from the characteristics and behavior of solid CO<sub>2</sub> on  
35 Mars, which are unlike those for any natural ice on Earth. In this paper, we present a  
36 model that helps us to investigate these features and some of their possible formation  
37 mechanisms. Our main objectives are:

- 38 (1) To study the different sublimation processes that can occur during spring.

- 39 (2) To test the “cold jets” theory and see under which conditions the CO<sub>2</sub> slab can  
40 sublimate at its base.
- 41 (3) To try to understand why dark spots appear in some locations and not everywhere  
42 at the same time.
- 43 (4) To study the earliest seasonal dark spots and see how much time they need to form,  
44 and under which conditions. A case study was made of the Manhattan Island area  
45 at 85° S.
- 46 (5) To test and improve the scenarios of this “dark spots cycle” with our results.

## 47 2. Model description

### 48 2.1. General description

49 To simulate the detailed seasonal evolution of a layer of CO<sub>2</sub> ice at a given location  
50 on Mars, we have developed a 1D model able to compute the temporal evolution of a  
51 column composed of an underlying regolith, a CO<sub>2</sub> ice layer, and the atmosphere above.  
52 It is an extension of a 1D version of the General Circulation Model from Laboratoire  
53 de Meteorologie Dynamique (Forget *et al.* 1999). The model is fully described in the  
54 following sections.

55 In practice, the atmospheric model allows one to simulate a radiative convective equi-  
56 librium atmospheric profile and is used to compute the incident radiation on the surface  
57 and the sensible heat exchange between the surface and the atmosphere (see below). Be-  
58 low the surface, we have developed a model that solves heat exchange, radiative transfer  
59 and mass evolution equations in the CO<sub>2</sub> slab as well as in the regolith. We used a finite  
60 volume approach to solve the equations, with a timestep of 0.001 Martian day (89 s).  
61 The model takes into account the solar flux (0.1-5  $\mu\text{m}$ ), the incident thermal flux, the  
62 thermal emission, the sensible heat flux, the geothermal heat flux, and the latent heat  
63 flux when there is a phase transition (Fig. 1).

64 [Figure 1 about here.]

### 65 2.2. Vertical grid

66 The vertical computational grid used in our model is a dynamic layer grid where  
67 individual layers have distinct thermal and optical properties. Their total number is

68 fixed; therefore, the number of regolith layers is equal to the difference between the total  
 69 number of layers and the number of CO<sub>2</sub> ice layers which evolves with time as CO<sub>2</sub>  
 70 condenses and sublimates. When a layer sublimates totally, this layer disappears and  
 71 another layer of regolith is added at the bottom of the domain at the temperature of  
 72 the above layer. In the case of condensation, if the first layer is full of CO<sub>2</sub> ice, another  
 73 layer of CO<sub>2</sub> ice is added above it, and the last layer of regolith is removed. Tests  
 74 were performed to check the energy balance and showed that it has no effect on the  
 75 results. The layer thickness is set to 1 cm. Simulations with thinner layers showed no  
 76 significant change in the results. Since measured thermal inertias on Mars range from  
 77 30 to 2000 J s<sup>-1/2</sup> m<sup>-2</sup> K<sup>-1</sup>, the grid used had to be such that it captures diurnal and  
 78 annual thermal waves in such media. For the regolith part, the skin depth corresponding  
 79 to oscillation period P would be for an homogeneous (infinite) soil (volumetric specific  
 80 heat C and conductivity λ):

$$\delta_P = \frac{I}{C} \left( \frac{P}{\pi} \right)^{1/2} \quad (1)$$

81 If we want to take into account the seasonal thermal waves, we thus have to consider a  
 82 minimum depth of 0.13 m for I=30 and 8.69 m for I=2000 (C=10<sup>6</sup> J K<sup>-1</sup> m<sup>-3</sup>). In our  
 83 simulations, we thus use a 10 m thick surface composed of a thousand 1 cm layers.

### 84 2.3. Incident solar visible radiation

#### 85 2.3.1. Atmospheric dust scattering

86 Visible and near infra-red radiative effects of dust are taken into account by computing  
 87 the radiative transfer in two different bands: 0.1-0.5 and 0.5-5 μm with a Toon *et al.*  
 88 (1989) radiative transfer code. The Delta-Eddington approximation is applied in order  
 89 to better simulate the forward scattering peak of dust particles. We use the Ockert-Bell  
 90 *et al.* (1997) dust properties in our model. However, other dust properties could be used  
 91 if needed (e.g. Wolff *et al.* 2009).

92 [Figure 2 about here.]

93 Atmospheric dust scattering plays a major role when the sun is low on the horizon,  
 94 as is common in polar regions. In the case of the Manhattan Island area (85° S), the  
 95 solar zenith angle is never less than about 60°. More interestingly, Fig. 2 shows that the

96 solar zenith angle is never less than about  $85^\circ$  when the first dark spots appear around  
 97 Ls  $175^\circ$  (Kieffer *et al.* 2006; Aharonson *et al.* 2004).

98 [Figure 3 about here.]

99 Simulations with a Monte-Carlo code using a spherical geometry (Vincendon and Langevin  
 100 2010) show that at that time, for an atmospheric dust optical depth set to 0.1 (Vincendon  
 101 *et al.* 2008) and dust confined to the first 6 km of the cold polar atmosphere, at least  
 102 one half of the solar flux that reaches the surface is scattered by atmospheric dust. The  
 103 incidence angles of these photons can be very different from the incidence angle of the  
 104 direct solar beam. This is important since in the slab model, for instance, the Fresnel  
 105 reflection coefficient quickly rises from 0.5 to 1 for solar angles higher than  $85^\circ$  (Fig.  
 106 3). Simulations performed with the Monte-Carlo code give us the distribution of these  
 107 incidence angles for various solar angles. To simplify, we computed an effective incidence  
 108 angle for these photons by calculating an effective albedo due to specular reflection and  
 109 then derived the corresponding angle

$$R_{\text{eff}} = \frac{\int_0^{\frac{\pi}{2}} f(i)R(i)di}{\int_0^{\frac{\pi}{2}} f(i)di} \quad (2)$$

110 with  $R_{\text{eff}}$  the effective albedo,  $f(i)$  the fraction of photons reaching the surface with an  
 111 incidence angle  $i$  and  $R(i)$  the Fresnel reflection coefficient for an incidence angle  $i$ . In  
 112 our model, we calculate the penetration of photons from the direct flux with an incidence  
 113 angle equal to the solar angle, and the penetration of photons from the scattered flux  
 114 with this computed effective incidence angle. The incident solar flux can be nonzero  
 115 when the sun is below the skyline. For an atmospheric dust optical depth set to 0.1  
 116 and dust confined to the first 6 km of the atmosphere, solar flux cannot be neglected at  
 117 incidence angles up to  $95^\circ$  (at  $91^\circ$ , about 1 percent of the incoming solar flux reaches  
 118 the surface and at  $95^\circ$  it is less than 0.1 percent).

119 We tuned our model to fit with these simulation results when the solar zenith angle  
 120 is greater than  $90^\circ$ . The cosine of the solar zenith angle is also corrected to take into  
 121 account the spherical geometry and the refraction by the atmosphere (Forget *et al.* 1999):

$$\mu_0 = \frac{\sqrt{1224 \mu_0^2 + 1}}{35} \quad (3)$$

122 [Figure 4 about here.]



123 *2.3.2. Effect of slope*

124 We use the model developed by Spiga and Forget (2008) to compute the influence  
125 of the slope and its orientation on our results. This allows us to compute the direct  
126 incoming flux  $D$ , the scattered flux by the atmosphere  $S$  and the reflected flux from the  
127 neighboring terrains  $R$ .

$$F_0 = D + S + R \quad (4)$$

128 We introduce here  $\sigma_s$  which is the sky-view factor that quantifies the proportion of the  
129 sky in the half-hemisphere “seen” by the slope that is not obstructed by the surrounding  
130 terrains (assumed to be flat).

$$\sigma_s = \frac{1 + \cos(\theta)}{2} \quad (5)$$

131 where  $\theta$  is the inclination of the slope. The thermal incident flux is computed assuming  
132 that the atmospheric thermal radiation is isotropic

$$F_{th} = \sigma_s F_{th0} + (1 - \sigma_s)E \quad (6)$$

133 with  $F_{th0}$  the incident thermal flux that would reach a flat terrain,  $E$  the thermal flux  
134 emitted by the surrounding terrains.

135 *2.4. Solar flux penetration*

136 Two models have been used to test the different scenarios: a  $\text{CO}_2$  “snow” model  
137 assuming that  $\text{CO}_2$  is composed of scattering and absorbent grains and a  $\text{CO}_2$  “slab  
138 ice” model assuming that  $\text{CO}_2$  is an homogeneous absorbent medium. This latter model  
139 can be used to test different scenarios where the photon pathlengths are in the range of  
140 several tens of centimeters, as revealed in several areas by TES (Kieffer *et al.* 2000) and  
141 OMEGA (Langevin *et al.* 2007) observations. We ran the simulations with a  $\text{CO}_2$  ice  
142 density of  $1606 \text{ kg m}^{-3}$  (which corresponds to a  $\text{CO}_2$  ice without porosity).

143 *2.4.1.  $\text{CO}_2$  snow model*

144 In this model, the grain size is specified, and then remains constant during the sim-  
145 ulation rather than evolving with time. The mass fraction of dust grains in the  $\text{CO}_2$  ice  
146 can be specified. However, to simplify the computation, dust scattering was treated as  
147 if dust particles were surrounded by vacuum. As for the atmosphere, we use the Ockert-  
148 Bell *et al.* (1997) optical parameters. Based on Langevin *et al.* (2007) we assume that

149 H<sub>2</sub>O ice grain content is negligible in the areas where the Kieffer (2007) scenario is likely  
 150 to occur. CO<sub>2</sub> ice optical properties are taken from Quirico and Schmitt (1997) and  
 151 Schmitt *et al.* (1998). Radiative transfer within the CO<sub>2</sub> ice is calculated with a Toon  
 152 *et al.* (1989) radiative transfer code as in Williams *et al.* (2008). Our model uses Mie  
 153 theory for single scattering by individual snow grains, together with the Delta-Eddington  
 154 method for multiple scattering in a snowpack as in Warren *et al.* (1990), Hansen (1999)  
 155 and Kieffer *et al.* (2000). To compute the optical depth of CO<sub>2</sub> and dust at a given  
 156 wavelength, we assume

$$\tau_{\text{CO}_2} = \frac{3 M_{\text{CO}_2} Q_{\text{ext}}^{\text{CO}_2}}{4 \rho_{\text{CO}_2} r_{\text{eff}}^{\text{CO}_2}} \quad (7)$$

157

$$\tau_{\text{dust}} = \frac{3 M_{\text{CO}_2} q_{\text{dust}} Q_{\text{ext}}^{\text{dust}}}{4 \rho_{\text{dust}} r_{\text{eff}}^{\text{dust}}} \quad (8)$$

158 where  $M_{\text{CO}_2}$  is the mass of CO<sub>2</sub> ice,  $q_{\text{dust}}$  the mass fraction of dust,  $Q_{\text{ext}}$  the extinction  
 159 coefficient,  $\rho$  the density, and  $r_{\text{eff}}$  the effective radius. In our simulations we assume  
 160  $r_{\text{eff}}^{\text{dust}} = 1.5 \mu\text{m}$ ,  $\rho_{\text{dust}} = 2000 \text{ kg m}^{-3}$  and  $\rho_{\text{CO}_2} = 1606 \text{ kg m}^{-3}$ . Finally the radiative  
 161 transfer code returns the upward and downward fluxes at each level, which leads to

$$E_{\text{pen}}(z_2 - z_1) = F_{\text{up}}(z_2) - F_{\text{up}}(z_1) + F_{\text{down}}(z_1) - F_{\text{down}}(z_2) \quad (9)$$

162 with  $E_{\text{pen}}(z_2 - z_1)$  the radiative energy deposited between  $z_1$  and  $z_2$  in  $\text{W m}^{-2}$ ,  $F_{\text{up}}(z)$   
 163 the upward flux at depth  $z$ ,  $F_{\text{down}}(z)$  the downward flux the depth  $z$ .

#### 164 2.4.2. Translucent slab model

165 This model is an extreme case of the previous model, in which the CO<sub>2</sub> slab is an  
 166 homogeneous absorbent medium. As photons reach the surface, some are reflected (Fres-  
 167 nel reflection) and the others penetrate into the ice. The latter are absorbed following a  
 168 Beer-Lambert law. However, the way solar radiation penetrates and propagates in the  
 169 ice depends not only on the properties of the medium, but also on the wavelength. To  
 170 simplify the calculation we compute an effective CO<sub>2</sub> real optical index (Warren 1986;  
 171 Quirico and Schmitt 1997; Schmitt *et al.* 1998; Hansen 2005) and Beer-Lambert coef-  
 172 ficient so that the reflection only depends on the incidence angle and the absorption of  
 173 the solar radiation in the ice only depends on the distance covered by the photons. The  
 174 penetration of solar energy was calculated as

$$\int_0^\infty S_\lambda (1 - R_\lambda) e^{-p/l_\lambda} d\lambda \quad (10)$$

175 where  $S_\lambda$  is the incident solar flux at the surface at a certain wavelength,  $R_\lambda$  the Fresnel  
 176 reflection coefficient,  $p$  the path length from the surface along the refracted path and  
 177  $l_\lambda = \lambda / 4\pi n_i$  the absorption length. With these results, we computed an effective absorp-  
 178 tion coefficient  $k$  that does not depend on the wavelength and use it in our model. The  
 179 solar radiation reaches the regolith whose albedo is fixed (mean value in the visible). The  
 180 reflected fraction is partly absorbed on its way back and the rest escapes from the slab.  
 181 In theory, as it reaches the surface, some of the flux is reflected into the slab. However,  
 182 when the regolith albedo is low (less than 0.3 for instance) this effect is small. For this  
 183 reason, we do not take into account multiple reflections in the slab. Dust can also be  
 184 added in the slab (see Fig. 6) . We have for the Fresnel reflection

$$R = \frac{r_s^2 + r_p^2}{2} \quad (11)$$

185 where  $r_s$  is the Fresnel coefficient if the light is polarized with the electric field perpen-  
 186 dicular to the incident plane and  $r_p$  the Fresnel coefficient if the light is polarized with  
 187 the electric field parallel to the incident plane.

$$r_s = \frac{n_{\text{atm}} \cos(\theta_{\text{inc}}) - n_{\text{CO}_2} \cos(\theta_{\text{ref}})}{n_{\text{atm}} \cos(\theta_{\text{inc}}) + n_{\text{CO}_2} \cos(\theta_{\text{ref}})} \quad (12)$$

$$r_p = \frac{n_{\text{atm}} \cos(\theta_{\text{ref}}) - n_{\text{CO}_2} \cos(\theta_{\text{inc}})}{n_{\text{atm}} \cos(\theta_{\text{ref}}) + n_{\text{CO}_2} \cos(\theta_{\text{inc}})} \quad (13)$$

189 with  $n_{\text{atm}} = 1$  and  $n_{\text{CO}_2} = 1.4$  (mean value in the visible (Warren 1986; Quirico and  
 190 Schmitt 1997; Schmitt *et al.* 1998; Hansen 2005).  $\theta_{\text{inc}}$  and  $\theta_{\text{ref}}$  are respectively the  
 191 incident angle and the refracted angle, which are linked by the relation

$$n_{\text{atm}} \sin(\theta_{\text{inc}}) = n_{\text{CO}_2} \sin(\theta_{\text{ref}}) \quad (14)$$

192 For an incident flux,  $F_0$

$$F_{\text{pen}}(1) = F_0(1 - R) \quad (15)$$

193 where  $R$  is the reflection coefficient for unpolarized light,  $F_{\text{pen}}(1)$  the flux that penetrates  
 194 into the first layer in  $\text{W m}^{-2}$  and  $F_0$  the incident flux in  $\text{W m}^{-2}$ . For the following layers,  
 195 with  $z_1$  and  $z_2$ , two different depths under the surface, and  $z_1 < z_2$ :

$$F_{\text{pen}}(z_2) = F_{\text{pen}}(z_1) e^{\left(\frac{-k(z_2 - z_1)}{\cos(\theta_{\text{ref}})}\right)} \quad (16)$$

196 with  $F_{\text{pen}}(z)$  the flux that penetrates into a surface at a depth  $z$  in  $\text{W m}^{-2}$ , and  $k$   
 197 a constant depending on the properties of the material between  $z_1$  and  $z_2$ . Kieffer  
 198 (2007) also computes the flux that reaches the regolith with respect to the depth and the  
 199 incidence angle. Our results are consistent with theirs.

200 After solar radiation reaches the regolith, one fraction is reflected and the other penetrates  
 201 into the regolith where it is absorbed in the first millimeters. We set the reflected angle  
 202 to  $45^\circ$ , the average angle for a lambertian reflection (see e.g. Vincendon *et al.* (2007),  
 203 Fig. 1). The reflected fraction is then partly absorbed into the ice before reaching the  
 204 surface. We thus have at the interface between  $\text{CO}_2$  ice and regolith

$$F_{\text{penref}}(z_{\text{interface}}) = F_{\text{pen}}(z_{\text{interface}})A_{\text{grd}} \quad (17)$$

205 and

$$F_{\text{penref}}(z_1) = F_{\text{penref}}(z_2)e^{\left(\frac{-k(z_2-z_1)}{\cos(\theta_{\text{ref}})}\right)} \quad (18)$$

206 with  $z_{\text{interface}}$  the depth of the interface between  $\text{CO}_2$  ice and the regolith in m,  $A_{\text{grd}}$  the  
 207 regolith albedo,  $F_{\text{penref}}(z)$  the reflected flux that penetrates into a surface at a depth  $z$   
 208 in  $\text{W m}^{-2}$ .

209

210 At the end we have:

$$E_{\text{pen}}(z_2 - z_1) = (F_{\text{pen}}(z_1) - F_{\text{pen}}(z_2)) + (F_{\text{penref}}(z_1) - F_{\text{penref}}(z_2)) \quad (19)$$

211 with  $E_{\text{pen}}(z_2 - z_1)$  the radiative energy deposited between  $z_1$  and  $z_2$  in  $\text{W m}^{-2}$ .

### 212 2.4.3. Synthesis

213 Figure 5 shows the reflected and absorbed fluxes in the two models. When we increase  
 214 the grain size in the  $\text{CO}_2$  snow model, the albedo decreases. More energy is absorbed  
 215 by the ice plus regolith. When the size is over a few centimeters, the solar radiation can  
 216 reach the regolith and the part of the flux that is absorbed in the ice decreases. The slab  
 217 ice model appears to be a good way to simulate pathlengths in the range of several tens  
 218 of centimeters.

219

[Figure 5 about here.]

220 For both models, we compute the energy that is absorbed in each layer and with that  
 221 result, we calculate the temperature increase between  $z_1$  and  $z_2$

$$\frac{\partial T}{\partial t} = \frac{E_{\text{pen}}}{\rho C_p (z_2 - z_1)} \quad (20)$$

222 with  $E_{\text{pen}}$  the radiative energy deposited between  $z_1$  and  $z_2$  in  $\text{W m}^{-2}$ ,  $C_p$  the heat  
 223 capacity of the layer in  $\text{J K}^{-1} \text{kg}^{-1}$ ,  $\rho$  the density,  $z_2 - z_1$  the thickness of the layer in m

224 [Figure 6 about here.]

225 However, the pressure is not constant within the slab, which is a critical point with  
 226 regards to the phase transition (see section 2.9).

## 227 2.5. Thermal infrared radiation absorption and emission

### 228 2.5.1. Downward atmospheric thermal flux

229 Gaseous  $\text{CO}_2$  and airborne dust emit a thermal flux that reaches the surface. This  
 230 thermal flux cannot penetrate more than a few millimeters into the  $\text{CO}_2$  ice (Kieffer  
 231 2007). In our model, it is treated as surface absorption.

### 232 2.5.2. Thermal emission

233 Thermal emission is equal to  $\epsilon \sigma T_{\text{surf}}^4$  with  $\sigma$  the Stephan-Boltzmann constant ( $\sigma = 5.67$   
 234  $10^{-8} \text{ W m}^{-2} \text{ K}^{-4}$ ),  $T_{\text{surf}}$  the surface temperature and  $\epsilon$  the spectrally averaged emissivity.  
 235 We set  $\epsilon = 0.9$  in the case of  $\text{CO}_2$  ice covering the soil and  $\epsilon = 0.95$  when there is no  
 236  $\text{CO}_2$  ice (Forget *et al.* 1998). Surface temperature  $T_{\text{surf}}$  is determined assuming that  
 237  $\text{CO}_2$  frost at the surface is in vapor pressure equilibrium with atmospheric  $\text{CO}_2$  gas at  
 238 surface pressure  $P_{\text{surf}}$  assuming a  $\text{CO}_2$  mixing ratio of 95%.

## 239 2.6. Sensible heat flux

240 The sensible exchange of heat between the surface and the atmosphere is calculated as  
 241 the product between the vertical gradient of temperature (estimated between the surface  
 242 value and that in the first atmospheric layer), the surface drag coefficient (computed  
 243 assuming a roughness length of 1 cm), and the wind velocity in the lowest level. This  
 244 velocity is estimated using the boundary layer scheme described in Forget *et al.* (1999),  
 245 assuming that the background wind velocity in the free atmosphere is  $10 \text{ m s}^{-1}$ . In

246 practice the sensible heat flux is very small because of the low density of the Martian  
247 atmosphere and the fact that the horizontal advection of heat is neglected.

### 248 2.7. Geothermal flux

249 Geothermal flux is set to a constant upward heat flux of  $0.030 \text{ W m}^{-2}$ , though esti-  
250 mates vary by a few  $\text{mW m}^{-2}$  (Schubert *et al.* 1992). The order of magnitude of this  
251 flux is generally negligible in the cumulative frost balance when compared with the other  
252 terms. Nevertheless, for facets in the shadow, it could accelerate the occurrence of the  
253 “crocus” day (i.e. the recession date) by typically one martian day.

### 254 2.8. Thermal conduction in ice and ground

255 For a solid, the time dependent diffusion equation leads to

$$\rho C_p \frac{\partial T}{\partial t} = -\nabla \vec{F}_c \quad (21)$$

256 where  $C_p$  is the specific heat (unit:  $\text{J kg}^{-1} \text{K}^{-1}$ ),  $\rho$  the material’s density in  $\text{kg m}^{-3}$ ,  $\vec{F}_c$  is  
257 the conductive heat flux:  $\vec{F}_c = -\lambda \vec{\nabla} T$  ( $\lambda$  is the solid’s heat conductivity, in  $\text{W m}^{-1} \text{K}^{-1}$ ).

$$\rho C_p \frac{\partial T}{\partial t} = \nabla [\lambda \nabla T] \quad (22)$$

258 Thermal conduction is here considered as a one dimensional (1D) process. Temperature  
259  $T$  of the soil is thus a function of time  $t$  and depth  $z$ , which must satisfy the following  
260 equation

$$\rho C_p \frac{\partial T}{\partial t} = \frac{\partial}{\partial z} \left( \lambda \frac{\partial T}{\partial z} \right) \quad (23)$$

261 In the context of physical processes in the soil, the boundary conditions for this  
262 problem are

$$-\lambda \frac{\partial T}{\partial z} (z = 0) + \Sigma F_{\text{other}} - \epsilon \sigma T^4 = 0 \quad (24)$$

263 at the surface and

$$-\lambda \frac{\partial T}{\partial z} (z = z_0) = F_{\text{geothermal}} \quad (25)$$

264 at the bottom of the domain.

265

266 Thermal conduction in the soil is computed as follows:

- 267 • Time integration is done via an implicit (first order) Euler scheme which approxi-  
268 mates the differential equation  $dT(t)/dt = F(T, t)$  as:

$$\frac{T^{(i+1)} - T^{(i)}}{\delta t} = F(T^{(i+1)}, t^{(i+1)}) \quad (26)$$

269 where superscripts denote time levels and  $\delta t$  the time step.

- 270 • The lower boundary condition is included as such in the solver, but the upper  
271 boundary condition is not. Surface temperature is technically linked to atmospheric  
272 and ground processes which are coupled (via boundary condition in Eq. 24). Rather  
273 than solving the coupled problem, it is uncoupled in a way that allows one to solve  
274 atmospheric and ground processes separately. The essential feature of the artificial  
275 uncoupling is that the atmospheric problem is first solved, yielding in the processes  
276 the value of surface temperature  $T_{\text{surf}}^{(i+1)}$  at time  $t^{(i+1)}$ , which is then used as an  
277 input boundary condition for the soil heat diffusion problem.

## 278 2.9. $\text{CO}_2$ phase transition

### 279 2.9.1. Sublimation temperature

280  $\text{CO}_2$  condensation/sublimation temperature is taken from Hourdin *et al.* (1993).  
281 This relation tends to slightly underestimate the sublimation temperature in the pressure  
282 range compared to other relations (James *et al.* 1992). However a maximum difference  
283 of 2 K was noticed and simulation results are not significantly impacted.

$$T_{\text{sub}}(z) = \frac{1}{0.0734 - 0.000324 \log(0.01 P_{\text{CO}_2}(z))} \quad (27)$$

284 with  $P_{\text{CO}_2}$  the partial pressure of  $\text{CO}_2$  in Pa. We take  $P_{\text{CO}_2} = 0.95 P_{\text{surf}}$  at the surface.  
285 We assume that the pressure inside the slab at depth  $z$  is given by:

$$P_{\text{CO}_2}(z) = P_{\text{surf}} + \rho g z \quad (28)$$

286 with  $\rho$  the density of the ice in  $\text{kg m}^{-3}$ ,  $g$  the gravity on Mars ( $3.72 \text{ m s}^{-2}$ ) and  $z$  the  
287 depth in m. Figure 7 shows the evolution of the sublimation temperature with depth. In  
288 our case,  $\text{CO}_2$  ice thickness can range from 10 cm at mid-latitudes to more than 70 cm  
289 in the polar regions. The difference between the sublimation temperature at the surface  
290 and the one at the bottom of the slab can be higher than 20 K in typical polar conditions.

291 [Figure 7 about here.]

292 *2.9.2. CO<sub>2</sub> sublimation/condensation*

293 Latent heat is released or absorbed as CO<sub>2</sub> condenses or sublimates such that:

$$L = -\frac{dm_{\text{CO}_2}}{dt} L_{\text{sub}}^{\text{CO}_2} \quad (29)$$

294 with  $L_{\text{sub}}^{\text{CO}_2}$  the CO<sub>2</sub> latent heat of sublimation ( $L_{\text{sub}}^{\text{CO}_2}=5.9 \cdot 10^5 \text{ J kg}^{-1}$ ) and  $m_{\text{CO}_2}$  the  
 295 mass of CO<sub>2</sub>. For each layer, the difference between the temperature of the layer, after  
 296 adding the increase due to solar energy absorption and computing conduction, and the  
 297 sublimation temperature leads us to the amount of CO<sub>2</sub> ice that sublimates (if CO<sub>2</sub> ice  
 298 is present) or condenses (if CO<sub>2</sub> gas is available):

$$dm_{\text{CO}_2}(i) = \frac{T_{\text{sub}}(i) - T_{\text{soil}}(i)}{L_{\text{sub}}^{\text{CO}_2} \Delta t} \rho C_p \Delta z(i) \quad (30)$$

299 where  $dm_{\text{CO}_2}(i)$  is the CO<sub>2</sub> mass variation in  $\text{kg s}^{-1} \text{ m}^{-2}$ ,  $T_{\text{soil}}(i)$  the predicted temper-  
 300 ature (without taking into account the phase transition) in layer  $i$  in K,  $T_{\text{sub}}(i)$  the subli-  
 301 mation temperature in K,  $\Delta t$  the timestep in s,  $C_p$  the CO<sub>2</sub> heat capacity in  $\text{J K}^{-1} \text{ kg}^{-1}$ ,  
 302  $\Delta z(i)$  the thickness of layer  $i$  in m. We actually compare the temperature of the layer,  
 303 which is calculated at the middle of the layer, with the sublimation temperature, which  
 304 is calculated at the base of the layer (or at the top of the layer for the first one, since  
 305 sublimation occurs at the surface). Decreasing the thickness of the layers shows that this  
 306 approximation had no significant effect on the results.

307 *2.10. Algorithm*

308 As we said previously, our model solves heat, radiation and mass evolution equations  
 309 in the CO<sub>2</sub> ice and in the regolith. If we consider a translucent slab, solar radiation can  
 310 easily penetrate. The regolith quickly heats and so does the CO<sub>2</sub> ice at the bottom of the  
 311 slab. If the sublimation temperature is reached, we first need to convert the energy in  
 312 excess to the amount of CO<sub>2</sub> that sublimates before computing the thermal conduction  
 313 in the above layers. Thus we need to couple heat, radiation and mass evolution. The  
 314 algorithm that we chose consists in computing the solar energy deposition in each layer,  
 315 then doing a loop with the following processes:

- 316 1. Find the layer where the excess of energy is the highest compared to the sublimation  
 317 point (or the lack of energy if we consider CO<sub>2</sub> layer where CO<sub>2</sub> gas is present, like



318 the first layer for instance). It is the layer where sublimation (or condensation) is  
 319 the most likely to occur.

- 320 2. Compute the latent heat related to this sublimation (or condensation).
- 321 3. Calculate the new thermal conduction coefficients and compute the new tempera-  
 322 tures.
- 323 4. Return to step 1. as long as there is still an excess of energy (or a lack in the  
 324 specified conditions).

325 These fluxes will be used later to calculate the sublimated or condensed amounts of CO<sub>2</sub>  
 326 ice in each layer. Calculating processes this way guarantees that the thermal conduction  
 327 is computed using realistic temperatures in the CO<sub>2</sub> ice that are never higher than the  
 328 sublimation point.

### 329 2.11. Effect of gas in the layers

330 If basal sublimation occurs, a layer of gas forms between the CO<sub>2</sub> slab and the  
 331 regolith, which modifies the thermal behavior of the slab. The conductivity of CO<sub>2</sub>  
 332 gas is much lower than the conductivity of CO<sub>2</sub> ice ( $\lambda_{\text{ice}}^{\text{CO}_2} = 0.65202 \text{ W m}^{-1} \text{ K}^{-1}$  at  
 333 144K,  $\lambda_{\text{gas}}^{\text{CO}_2} = 0.00590 \text{ W m}^{-1} \text{ K}^{-1}$  (Kieffer 2007)). Moreover, the distance between  
 334 the ice and the regolith will increase. Both radiation and convection can play a role  
 335 in the transfer of heat through this gaseous layer. We can simulate this behavior as  
 336 the conductive, radiative and convective transfer between two horizontal plates with the  
 337 temperature of the plate below higher than the temperature of the plate above. The  
 338 total flux of energy between the two plates is

$$\Sigma Flux = C_d + R_d + C_v \quad (31)$$

339 where  $C_d$  is the conductive flux,  $R_d$  the radiative flux and  $C_v$  the convective flux.

340 We can estimate

$$C_d = \lambda_{\text{gas}}^{\text{CO}_2} \frac{\partial T}{\partial z_{\text{gas}}} \quad (32)$$

341  $z_{\text{gas}}$  takes into account the gas expansion. For the radiative exchange, we suppose here  
 342 that  $\epsilon$  is equal to 1 for the CO<sub>2</sub> ice and for the regolith at the interface in order to  
 343 simplify the calculation:

$$R_d = \Delta(\sigma T^4) \quad (33)$$

344 where  $\sigma$  is the Stephan-Boltzmann constant and  $T$  the temperature at the regolith/CO<sub>2</sub>  
345 gas interface and at the CO<sub>2</sub> ice/CO<sub>2</sub> gas interface.

346 For the convective flux, we have first to determine the Rayleigh number ( $Ra$ ), which  
347 is the product of the Grashof number ( $Gr$ ) and the Prandtl number ( $Pr$ ).

$$Ra = Gr Pr \quad (34)$$

$$Gr = \frac{g\beta\Delta T\Delta z_{\text{gas}}^3}{\nu^2} \quad (35)$$

348

$$Pr = \frac{C_p \mu}{\lambda} \quad (36)$$

349 where  $\nu$  is the kinematic viscosity of CO<sub>2</sub>,  $\beta$  the volumetric thermal expansion coefficient  
350 (equal to approximately 1/T for ideal fluids, where T is the temperature),  $g$  the gravity  
351 on Mars and  $\Delta z_{\text{gas}}$  the distance between the regolith/CO<sub>2</sub> gas interface and the CO<sub>2</sub>  
352 ice/CO<sub>2</sub> gas interface.  $\nu = \frac{\mu}{\rho}$  where  $\mu$  is the CO<sub>2</sub> gas viscosity (1.1 10<sup>-5</sup> Pa s at 160 K)  
353 and  $\rho$  the CO<sub>2</sub> gas density (0.125 kg m<sup>-3</sup> at 162.8 K under a 0.6 m thick CO<sub>2</sub> ice slab  
354 for surface pressure equal to 507 Pa). We can estimate

$$Ra = 4.81 * 10^6 \Delta T \Delta z_{\text{gas}}^3 \quad (37)$$

355 Since we are in the case of Rayleigh-Benard convection, the critical value of the Rayleigh  
356 number is estimated at 1707. We can assume a reasonable gas layer width of 2 cm  
357 (Kieffer 2007). In this case, the critical value is obtained for  $\Delta T=44\text{K}$ , which is one  
358 order of magnitude above the modeled gradient. We therefore assumed in our study that  
359 convection could be neglected.

360 To compute the effect of gas in the layer using the conduction equation (Eq. 22), we  
361 kept the calculation as before, as if the ice and the regolith were in conductive contact,  
362 but used an equivalent conductivity between them which takes into account

363 (1) the expansion of the gas and its conductivity

364 (2) the radiative flux.

365 We have

$$\lambda_{\text{eqgas}} \frac{\Delta T}{(1 - q_{\text{CO}_2})\Delta z} = \lambda_{\text{gas}} \frac{\Delta T}{(1 - q_{\text{CO}_2})\gamma\Delta z} + \sigma\Delta(T^4) \quad (38)$$

366 where  $\gamma$  is the expansion coefficient of CO<sub>2</sub> ( $\gamma = \frac{\rho_{\text{solid}}}{\rho_{\text{gas}}}$ ) and  $q_{\text{CO}_2}$  the fraction of solid  
367 CO<sub>2</sub> in the layer. Rearranging,

$$\lambda_{\text{eqgas}} = \frac{\lambda_{\text{gas}}}{\gamma} + (1 - q_{\text{CO}_2})\Delta z\sigma \frac{\Delta(T^4)}{\Delta T} \quad (39)$$

368 When basal sublimation occurs, the last layer of CO<sub>2</sub> has both ice and gas. We have to  
369 calculate its new conductivity, which is given by

$$\lambda_{\text{eq}} = \frac{\Delta z}{\frac{q_{\text{CO}_2}\Delta z}{\lambda_{\text{solid}}} + \frac{(1-q_{\text{CO}_2})\Delta z}{\lambda_{\text{eqgas}}}} \quad (40)$$

### 370 2.12. Gas ejection

371 In our model, we assume that in case of basal sublimation, when the gas amount  
372 reaches a threshold value (which can be chosen), the ice breaks, the gas is ejected in  
373 the atmosphere and the amount of gas at the base of the CO<sub>2</sub> slab is set to zero. This  
374 threshold value is set to 2 cm in the simulations, a reasonable value according to Kieffer  
375 (2007). However, it has no significant impact since it corresponds to a very small amount  
376 of gas which can form in only a few hours. Assuming no heat exchange during the ejection  
377 we have

$$\frac{T_{\text{exit}}}{T_{\text{soil}}(z)} = \left(\frac{P_{\text{surf}}}{P(z)}\right)^{\left(\frac{R_{\text{CO}_2}}{C_p}\right)} \quad (41)$$

378 where  $T_{\text{exit}}$  is the temperature of the gas when it is ejected in the atmosphere,  $T_{\text{soil}}(z)$  the  
379 temperature at the depth  $z$  where CO<sub>2</sub> ice is sublimated,  $P_{\text{surf}}$  the surface pressure,  $P(z)$   
380 the pressure of the gas at the depth  $z$  where CO<sub>2</sub> ice is sublimated,  $R_{\text{CO}_2}$  the specific  
381 gas constant of CO<sub>2</sub>,  $C_p$  the specific heat of CO<sub>2</sub> gas. Let us take a typical example  
382 with a 0.6 m thick CO<sub>2</sub> slab. Pressure at the base is close to 3985 Pa if the surface  
383 pressure is equal to 400 Pa (a typical surface pressure at 85° S latitude and Ls 180°).  
384 The temperature at the base of the slab is equal to the sublimation temperature in these  
385 conditions, i.e. 162.75 K. The calculation gives us an ejection temperature close to 98 K  
386 which means that, using this simple approach, we can estimate that about 7 percent of  
387 the ejected gas may recondense during the ejection:

$$\% \text{ of recondensation} = \frac{T_{\text{cond}} - T_{\text{exit}}}{L_{\text{cond}}^{\text{CO}_2}} C_p^{\text{gas}} \quad (42)$$

### 388 3. Results and application to the Manhattan Island region

#### 389 3.1. The Manhattan Island region

390 The “Manhattan Island” region is centered at  $99^\circ$  E,  $86.25^\circ$  S, and follows the classic  
391 TES “cryptic” behavior of low albedo while remaining near the  $\text{CO}_2$  ice temperature  
392 (Kieffer *et al.* 2006). At this latitude, polar night begins at  $\text{Ls } 10^\circ$  and ends at  $\text{Ls } 168^\circ$ .  
393 The first dark spots appear very quickly after the end of the polar night. They can be  
394 seen in THEMIS images at  $\text{Ls } 176^\circ$  (Kieffer *et al.* 2006). In this region, OMEGA spectra  
395 show that  $\text{CO}_2$  ice consists of a thick slab, contaminated by dust in the upper layers  
396 (Langevin *et al.* 2007). This spectrum is typical of the cryptic region. OMEGA data  
397 were acquired between  $\text{Ls } 183^\circ$  and  $\text{Ls } 192^\circ$  and since dust may have been brought by  
398 the venting process, it is possible that a clean slab lay on the ground earlier, at the end  
399 of the polar night. According to our model, such a slab would be very translucent in the  
400 visible. For instance, with a solar incidence angle of  $70^\circ$ , about  $3/4$  of the flux reaches  
401 the base of the slab. We thus tried our model with this particular area. The main point  
402 here was to check if basal sublimation could occur and when.

#### 403 3.2. Evolution of temperature

404 The following baseline parameters were chosen: slab model; uniform regolith thermal  
405 inertia: 200 SI; regolith albedo: 0.24; atmospheric dust optical depth: 0.1 (Vincendon *et*  
406 *al.* 2008; Vincendon *et al.* 2009).

##### 407 3.2.1. Simulation results on a flat terrain:

408 [Figure 8 about here.]

409 [Figure 9 about here.]

410 Just after the end of the polar night, as the sun is low on the horizon, the Fresnel  
411 reflection severely limits the direct solar flux penetration and temperatures remain near  
412  $145$  K in the slab, as shown in Fig. 8. The total amount of  $\text{CO}_2$  ice keeps growing even  
413 if sublimation at the surface has already begun during the day. As soon as the sun is  
414 high enough in the sky, solar radiation penetrates down to the regolith interface where it  
415 is absorbed in the first few millimeters. Temperature increases quickly, and by thermal

416 conduction, at the base of the CO<sub>2</sub> slab. Sublimation temperature at the base of the  
417 slab is reached at Ls 191 °, during the afternoon. The ejection time occurs a few tens  
418 of minutes after the sublimation begins. Gas continues to form and to be vented out  
419 until the night comes and the temperature gets too low. The simulation results show  
420 that some energy is kept during the night in the slab. Therefore, each following day the  
421 energy that is needed for basal sublimation to occur decreases and the first gas ejection  
422 of the day is earlier than for the previous day. As shown by Fig. 8, adding dust, even  
423 a few ppm, has a significant impact on the results. Dust radically changes the slab's  
424 properties. For instance, a slab with a mass fraction of dust of 10 ppm absorbs about 5  
425 time more solar radiation. That is the reason why temperature is higher in the slab when  
426 dust is present. However, a smaller fraction of solar radiation can reach the regolith and  
427 temperature increase at the interface is slower. "Crocus" day occurs at about Ls 245 ° in  
428 these simulations, which is quite early compared to the observations (more in the range  
429 of Ls 250-280 °) (Kieffer *et al.* 2000; Langevin *et al.* 2007). We have to keep in mind  
430 that we simulate here a slab with constant properties, as we are mainly interested in  
431 simulating the onset of spot formation. In reality dust and CO<sub>2</sub> frost that are ejected  
432 change the optical properties of the slab. This optically thick layer of dust and frost stops  
433 the solar radiation and sublimation can occur only at the surface until wind removes this  
434 dust away and frost sublimates. Solar radiation can then penetrate in the slab again and  
435 basal sublimation can go on. After the "crocus" day, the surface temperature increases  
436 very quickly up to about 260 K as shown by Fig. 9. During fall, the surface temperature  
437 decreases down to the condensation point and CO<sub>2</sub> ice begins to form.

438 *3.2.2. Simulation results on a 30 ° north oriented slope:*

439 [Figure 10 about here.]

440 [Figure 11 about here.]

441 For these simulations, we took into account a 30 ° north oriented slope (equator fac-  
442 ing). Processes involved in this simulation (Fig. 10 and 11) are quite similar to the  
443 previous one. However, since the angle between the direct incoming solar flux and the  
444 local vertical is slightly lower, Fresnel reflection is not that significant and a large part of  
445 the solar radiation can penetrate very early into the slab. As a result, first gas ejections

446 can occur as early as Ls 174° which is consistent with the observations. We can notice  
447 (Fig. 10) that at Ls 174° (12 AM), gas ejection has not yet occurred (it will occur a few  
448 hours later). As for the flat terrain case, each day, the first gas ejection occurs earlier  
449 than for the previous day; at Ls 180°, the gas ejection already occurred. Since the gas  
450 layer acted like an insulator, energy was kept in the first regolith layers and was released  
451 after the gas ejection. This 30° north oriented slope case can actually be seen as a good  
452 way to represent a small-scale irregularity on a flat terrain.

#### 453 4. Dark spots formation on Mars

454 We have shown in the previous section that basal sublimation could occur in the  
455 Manhattan Island area. We then investigated more general cases and tried to see how  
456 significant the different parameters are for initiating the venting process.

##### 457 4.1. Mean effective grain size and the dust content

458 CO<sub>2</sub> ice properties are the key to the venting process. Figure 12 shows that different  
459 scenarios will occur, depending on these properties (CO<sub>2</sub> ice grain size and dust content).  
460 In every case, sublimation occurs at the surface, but if solar radiation can penetrate deep  
461 in the ice, basal sublimation becomes possible.

462 [Figure 12 about here.]

##### 463 4.1.1. Surface sublimation

464 Very clean small-grained ice has an albedo so high that there is not enough energy  
465 to entirely sublime the seasonal CO<sub>2</sub> ice layer and ice accumulates year after year (Fig.  
466 12, zone 4). If we increase the grain size or add dust (Fig. 12, zone 3), we decrease the  
467 albedo and a CO<sub>2</sub> cycle consistent with the observed one is possible. Figure 13 shows  
468 that the temperature remains near 145 K in the CO<sub>2</sub> slab until the “crocus” day. Solar  
469 radiation is absorbed in the first millimeters and sublimation only occurs at the surface.

470 [Figure 13 about here.]

471 *4.1.2. Sublimation within the ice*

472 If we continue to increase the effective grain size (more than a few millimeters) and  
473 limit the mass fraction of dust to less than a few hundreds of ppm (Fig. 12, zone 2),  
474 solar radiation begins to penetrate more deeply into the ice. Still, most of the energy is  
475 absorbed by the ice and very little can reach the regolith. Sublimation temperature can  
476 be reached within the ice, as shown on Fig. 14 and Fig. 15. CO<sub>2</sub> gas bubbles can form  
477 around and ice could eventually crack.

478 [Figure 14 about here.]

479 [Figure 15 about here.]

480 *4.1.3. Basal sublimation*

481 When the effective grain size is in the range of about ten centimeters or more, and  
482 the mass fraction of dust is less than about 10 to 15 ppm (Fig. 12, zone 1), the fraction  
483 of solar radiation that reaches the regolith is sufficient for basal sublimation to occur.  
484 As we explained before, surface sublimation continues at the same time.

485 *4.1.4. Diurnal cycle*

486 Slab CO<sub>2</sub> ice and small grained CO<sub>2</sub> ice have totally different behaviors with regard  
487 to the diurnal cycle, as can be seen on Fig. 16 and Fig. 17. With small grained CO<sub>2</sub>  
488 ice, everything occurs at the surface, where the CO<sub>2</sub> ice layer is in equilibrium with the  
489 atmosphere and the CO<sub>2</sub> ice amount evolution is directly linked to the diurnal cycle. It  
490 decreases during the day and increases during the night. However, in the case of the  
491 translucent slab scenario, the diurnal cycle has less influence on the sublimation and  
492 condensation processes. Only a small fraction of the solar flux is absorbed by the CO<sub>2</sub>  
493 ice. Most of the energy is absorbed by the regolith. Thus during the day, sublimation at  
494 the surface is limited. Thermal conduction, but also solar flux absorption in the CO<sub>2</sub> ice,  
495 leads to energy storage in the slab and condensation during the night is reduced (Fig.  
496 17).

497 [Figure 16 about here.]

498 [Figure 17 about here.]

499

[Figure 18 about here.]

500 *4.2. Effect of slope and orientation*

501 Slope and orientation change the incidence angle of the photons, and therefore the  
502 Fresnel reflection which limits the solar flux penetration. At high latitudes, the solar  
503 zenith angle is generally between  $80^\circ$  and  $90^\circ$  at the beginning of spring. Slope and  
504 orientation thus determine when a large fraction of the solar radiation begins to penetrate  
505 into the slab and thus when the first gas ejection will occur. In the case of Manhattan  
506 Island ( $85^\circ$  S), Fig. 18 shows that the  $\text{CO}_2$  ice maximum is about 15% smaller on a  
507  $30^\circ$  north oriented slope than on a flat terrain, and the sublimation temperature at the  
508 base of the slab is therefore about 1 K lower. Furthermore, at  $\text{Ls } 175^\circ$  for instance, solar  
509 zenith angle minimum is at about  $86^\circ$  (Fig. 2), which means that a maximum of 40%  
510 of the direct flux can penetrate into the slab for a flat terrain whereas more than 90%  
511 penetrates in the case of a  $30^\circ$  north oriented slope.

512 *4.3. Regolith thermal inertia*

513 Aharonson (2004) and Kieffer (2007) suggested that the seasonal thermal wave could  
514 be sufficient to cause  $\text{CO}_2$  ice sublimation during the polar night. We did not observe any  
515 gas ejection in our simulations during the polar night, even when we considered a high  
516 thermal inertia (up to 2000 SI) that could be representative of an ice-rich near-surface.  
517 High thermal inertia certainly limits the  $\text{CO}_2$  condensation but also makes the regolith  
518 heating much more difficult. Since the sublimation temperature at the interface is much  
519 greater than at the surface it is very difficult to reach it. Figure 19 shows that increasing  
520 the thermal inertia of the regolith delays by up to  $10^\circ$  of  $\text{Ls}$  the starting date of  $\text{CO}_2$  jet  
521 activity. Seasonal thermal waves can therefore not initiate the venting process on their  
522 own. Furthermore, according to our results, regolith thermal inertia does not have a large  
523 impact on the time of the first gas ejection (a few degrees of  $\text{Ls}$ ) since both previously  
524 mentioned processes seem to compensate each other.

525

[Figure 19 about here.]



#### 526 4.4. Regolith albedo

527 We ran tests with albedo values between 0.05 and 0.3 (realistic range for the martian  
528 soil). Figure 20 shows a small increase (less than 5 ° of Ls for the albedo range) of the  
529 time needed to heat up the regolith as we increased the albedo.

530 [Figure 20 about here.]

#### 531 4.5. Latitude

532 Simulations were also run at different latitudes (Fig. 21). Atmospheric dust optical  
533 depth was kept to 0.1. Surface pressure was set to 400 Pa in the southern hemisphere  
534 and to 1000 Pa in the northern hemisphere. This higher pressure in the north tends  
535 to increase the maximum amount of CO<sub>2</sub> ice. This explains why CO<sub>2</sub> ice maxima are  
536 rather close in north and south polar regions in spite of the fact that the southern polar  
537 night is longer. The time of initiation of the venting process evolves with latitude, as a  
538 function of the incident solar radiation.

539 [Figure 21 about here.]

## 540 5. Discussion

### 541 5.1. Manhattan Island region scenario

542 CO<sub>2</sub> ice may have some dust inclusions when the first solar beams penetrate, about  
543 10 ° of Ls before the end of the polar night. The solar radiation remains too low to  
544 significantly heat the regolith at that time, but its heating may clean the slab, as described  
545 in Kieffer (2007) and Portyankina *et al.* (2010). Thus, at the end of the polar night, when  
546 the solar radiation is significantly higher, the slab is probably translucent and the clean  
547 slab scenario is appropriate. A large fraction of solar radiation can penetrate as soon  
548 as polar night ends on small-scale irregularities (equator facing slopes) and initiates the  
549 venting process. The regolith quickly heats up and sublimation temperature is reached  
550 at the base of the CO<sub>2</sub> slab as early as Ls 174 °. During the day, gas continues to form  
551 and to be ejected. At night, sublimation stops until the following day when sublimation  
552 temperature can be reached again. When frost and dust cover the ice, solar radiation  
553 cannot penetrate as easily anymore. However, basal sublimation can continue outside

554 the dark spot. As the slab has already been weakened by the first gas ejection, it is  
555 likely that sublimated CO<sub>2</sub> will try to escape by the same path. As the CO<sub>2</sub> ice amount  
556 decreases, pressure difference between the surface and the base of the slab decreases.  
557 Gas and dust ejection is therefore less and less violent and less and less dust or substrate  
558 material is expelled outside. Near Ls 260°, “crocus” day occurs: CO<sub>2</sub> disappears and  
559 regolith heats up to 260 K in a few days.

### 560 5.2. Venting process on Mars

561 Several areas with slab ice have been observed at different latitudes on Mars. Our  
562 simulations tend to show that for similar conditions, basal sublimation can occur at every  
563 latitude. Of course, the effect will not be the same at 85° S where there may be a 60 cm  
564 thick slab and at 50° S where it will not be thicker than 10 cm. Indeed the difference  
565 of pressure between the bottom of the slab and the surface will be totally different. At  
566 mid latitudes, where there is much less ice, gas ejection will be less energetic and there  
567 will be less (or no) ejected dust and substrate material. The main result is that as long  
568 as we have similar conditions (ice properties, albedo, regolith thermal inertia, etc.), gas  
569 ejections are as likely to occur in the north as in the south. Kieffer and Titus (2001)  
570 and Piqueux *et al.* (2008) report evidence of active venting processes in the north which  
571 confirm our results. However, water ice is much more abundant in north polar regions  
572 and certainly plays a role. Adding water ice inclusions in our model should allow us to  
573 investigate more deeply dark spot formation in these regions.

### 574 5.3. Dark spots on dunes

575 One interesting question with dark spots is that when we look at an area with dune  
576 fields, they often seem to appear only on dunes (see Fig. 2 in Kieffer (2007) and Fig.  
577 22 in this article). Can we explain this behavior with our model? Dunes have generally  
578 a lower albedo than the surrounding terrains (less than 0.2), a lower thermal inertia  
579 due to smaller grained material (as low as 50 SI) and present some slopes (Fig. 23).  
580 Model results show that gas ejections on the surrounding terrains should occur about  
581 10 to 20° of Ls after the ones on the dunes. The model cannot explain why dark spots  
582 seem to occur only on dunes. Whether gas ejection occurs or not is determined by CO<sub>2</sub>  
583 ice properties, which are expected to be similar both on dunes and the surroundings

584 (see previous sections). We think that gas ejections also occur around dunes but are  
585 much more difficult to detect due to differences in the substrate material. Dunes are  
586 composed of dark sand and the dust grains that cover the surrounding terrains have a  
587 higher albedo, as can be seen on Fig. 23. In the case of a gas ejection, some substrate  
588 material is brought up by the gas and ejected. The substrate material forms a dark spot  
589 surrounded by bright CO<sub>2</sub> frost. We thus suggest that gas ejections first occur on dunes  
590 and that dark and large spots appear. A little bit later, gas ejection begins to occur on  
591 surrounding terrains and dust is ejected. Considering the difference of albedo, it is more  
592 difficult to detect dust than dark sand on the CO<sub>2</sub> ice deposit. Still, in both cases bright  
593 patches due to CO<sub>2</sub> recondensation should form. The results that we present here are  
594 consistent with previous HiRISE observations of dunes fields (Fig. 24).

595 [Figure 22 about here.]

596 [Figure 23 about here.]

597 [Figure 24 about here.]

#### 598 5.4. Cracks within the ice

599 As explained previously, we found that the sublimation temperature could be reached  
600 within the CO<sub>2</sub> ice under certain conditions. We suggest the following interpretation for  
601 such a phenomenon: CO<sub>2</sub> gas bubbles form at the interfaces, which means around the  
602 dust, H<sub>2</sub>O and CO<sub>2</sub> small grains. Pressure around these interfaces increases and causes  
603 cracks in the ice. These cracks anneal during the cooler portion of the diurnal cycle,  
604 especially as the slab becomes cleaner following the likely ejection of the dust particles  
605 that induced them. This means that CO<sub>2</sub> ice properties do not remain constant: the  
606 CO<sub>2</sub> ice effective grain radius decreases as cracks appear within the ice. Figure 12 should  
607 therefore be seen as a dynamic diagram. CO<sub>2</sub> ice composition and properties evolve with  
608 time. For instance, if sublimation within the ice was possible at a given time, cracks  
609 would cause a decrease of the effective radius, leading to totally different ice properties.  
610 This mechanism could be a clue to understand the decrease of the mean effective grain  
611 radius observed during spring in some areas of the southern polar cap (Langevin *et al.*  
612 2007). Different ice properties would lead to different sublimation processes, that could

613 themselves change these ice properties. This interpretation is highly speculative and  
614 needs further study to be repudiated or confirmed, but raises an interesting concern  
615 about the CO<sub>2</sub> ice dynamics on Mars

## 616 6. Conclusion

617 (1) Only in the case of very large CO<sub>2</sub> grains and very little dust contamination, can  
618 a large fraction of solar radiation reach the regolith. In this latter case, the model  
619 shows that the regolith surface can heat and sublimation temperature at the base of  
620 the CO<sub>2</sub> ice can be reached, which is consistent with Kieffer (2007).

621 (2) Simulation results show that the occurrence of basal sublimation during spring only  
622 depends on the CO<sub>2</sub> ice properties, considering that the substrate on which the CO<sub>2</sub>  
623 ice lies has an albedo lower than 0.3. Other parameters (thermal inertia, slope angle),  
624 however, have a significant impact on the starting date of the jet activity.

625 (3) Early dark spot formation in Manhattan Island region (85° S) cannot be explained  
626 by seasonal thermal waves. However, our results show that the venting process can  
627 under certain conditions be initiated very early by solar radiation penetration and  
628 that dark spots could form as early as Ls 174°.

629 (4) We suggest that the venting process also occurs around the dunes. However, sub-  
630 strate material nature make them certainly difficult to observe compared to the dark  
631 spots on the dunes.

632 (5) We suggest that the decrease of the CO<sub>2</sub> ice effective grain radius observed during  
633 spring in some of the southern polar regions could be caused by cracks in the ice,  
634 which would be the result of sublimation within the ice.

635 In our simulations, we considered CO<sub>2</sub> ice with homogeneous and constant prop-  
636 erties (grain size, dust inclusions) through time. Adding the possibility to have non-  
637 homogeneous and evolving ice should allow us to investigate in the future the differences  
638 between the cryptic and in the anticryptic regions. Furthermore, better knowledge about  
639 the nature and properties of the CO<sub>2</sub> ice during winter and its evolution with time would  
640 also be required to improve the simulations.

641 **Acknowledgement**

642 We would like to thank B. Schmitt for making his optical CO<sub>2</sub> ice properties avail-  
643 able. We are also grateful to P.Y. Meslin, Y. Langevin, S. Douté, A. Spiga, and all our  
644 colleagues at LMD for inspiration and advice.

645 Aharonson, O., 2004. Sublimation at the Base of a Seasonal CO<sub>2</sub> Slab on Mars. In: Mackwell, S.,  
646 Stansbery, E. (Eds.), Lunar and Planetary Institute Science Conference Abstracts. Vol. 35 of Lunar  
647 and Planetary Institute Science Conference Abstracts. pp. 1918–+.

648 Bibring, J., Langevin, Y., Poulet, F., Gendrin, A., Gondet, B., Berthé, M., Soufflot, A., Drossart, P.,  
649 Combes, M., Bellucci, G., Moroz, V., Mangold, N., Schmitt, B., OMEGA team, t., 2004. Perennial  
650 water ice identified in the south polar cap of Mars. *Nature* 428, 627–630.

651 Forget, F., Hourdin, F., Fournier, R., Hourdin, C., Talagrand, O., Collins, M., Lewis, S. R., Read, P. L.,  
652 Huot., J.-P., 1999. Improved general circulation models of the Martian atmosphere from the surface  
653 to above 80 km. *J. Geophys. Res.* 104, 24,155–24,176.

654 Forget, F., Hourdin, F., Talagrand, O., 1998. CO<sub>2</sub> snow fall on Mars: Simulation with a general circu-  
655 lation model. *Icarus* 131, 302–316.

656 Hansen, G. B., 1999. Control of the radiative behavior of the Martian polar caps by surface CO<sub>2</sub> ice:  
657 Evidence from Mars Global Surveyor measurements. *J. Geophys. Res.* 104, 16471–16486.

658 Hansen, G. B., 2005. Ultraviolet to near-infrared absorption spectrum of carbon dioxide ice from 0.174  
659 to 1.8  $\mu\text{m}$ . *Journal of Geophysical Research (Planets)* 110, 11003–+.

660 Hourdin, F., Le Van, P., Forget, F., Talagrand, O., 1993. Meteorological variability and the annual  
661 surface pressure cycle on Mars. *J. Atmos. Sci.* 50, 3625–3640.

662 James, P. B., Kieffer, H. H., Paige, D. A., 1992. The seasonal cycle of carbon dioxide on Mars. In: Mars.  
663 University of Arizona Press, Tucson, pp. pp. 934–968.

664 Kieffer, H. H., 2007. Cold jets in the Martian polar caps. *J. Geophys. Res.* 112, 8005–+.

665 Kieffer, H. H., Christensen, P. R., Titus, T. N., 2006. CO<sub>2</sub> jets formed by sublimation beneath translucent  
666 slab ice in Mars' seasonal south polar ice cap. *Nature* 442, 793–796.

667 Kieffer, H. H., Titus, T. N., 2001. TES Mapping of Mars' North Seasonal Cap. *Icarus* 154, 162–180.

668 Kieffer, H. H., Titus, T. N., Mullins, K. F., Christensen, P. R., 2000. Mars south polar spring and summer  
669 behavior observed by TES: Seasonal cap evolution controlled by frost grain size. *J. Geophys. Res.* 105,  
670 9653–9700.

671 Langevin, Y., Bibring, J.-P., Montmessin, F., Forget, F., Vincendon, M., Douté, S., Poulet, F., Gondet,  
672 B., 2007. Observations of the south seasonal cap of Mars during recession in 2004-2006 by the OMEGA  
673 visible/near-infrared imaging spectrometer on board Mars Express. *J. Geophys. Res.* 112 (E11), 8–+.

674 Langevin, Y., Douté, S., Vincendon, M., Poulet, F., Bibring, J.-P., Gondet, B., Schmitt, B., Forget,  
675 F., 2006. No signature of clear CO<sub>2</sub> ice from the 'cryptic' regions in Mars' south seasonal polar cap.  
676 *Nature* 442, 790–792.

677 Malin, M. C., Edgett, K. S., 2000. Frosting and Defrosting of Martian Polar Dunes. In: Lunar and

- 678 Planetary Institute Science Conference Abstracts. Vol. 31 of Lunar and Planetary Inst. Technical  
679 Report. pp. 1056–+.
- 680 Ockert-Bell, M. E., Bell III, J. F., McKay, C., Pollack, J., Forget, F., 1997. Absorption and scattering  
681 properties of the Martian dust in the solar wavelengths. *J. Geophys. Res.* 102, 9039–9050.
- 682 Piqueux, S., Byrne, S., Richardson, M. I., 2003. Sublimation of Mars's southern seasonal CO<sub>2</sub> ice cap  
683 and the formation of spiders. *J. Geophys. Res.* 108, 5084–+.
- 684 Portyankina, G., Markiewicz, W. J., Thomas, N., Hansen, C. J., Milazzo, M., 2010. HiRISE observations  
685 of gas sublimation-driven activity in Mars southern polar regions: III. Models of processes involving  
686 translucent ice. *Icarus* 205, 311–320.
- 687 Quirico, E., Schmitt, B., 1997. A Spectroscopic Study of CO Diluted in N<sub>2</sub> Ice: Applications for Triton  
688 and Pluto. *Icarus* 128, 181–188.
- 689 Schmitt, B., Quirico, E., Trotta, F., Grundy, W. M., 1998. Optical Properties of Ices from UV to  
690 Infrared. In: B. Schmitt, C. de Bergh, & M. Festou (Ed.), *Solar System Ices*. Vol. 227 of *Astrophysics  
691 and Space Science Library*. pp. 199–+.
- 692 Schubert, G., Solomon, S. C., Turcotte, D. L., Drake, M. J., Sleep, N. H., 1992. Origin and thermal  
693 evolution of Mars. *Mars*, pp. 147–183.
- 694 Spiga, A., Forget, F., 2008. Fast and accurate estimation of solar irradiance on Martian slopes. *Geo-  
695 phys. Res. Lett.* 35 (L15201).
- 696 Supulver, K. D., Edgett, K. S., Malin, M. C., 2001. Seasonal Changes in Frost Cover in the Martian  
697 South Polar Region: Mars Global Surveyor MOC and TES Monitoring of the Richardson Crater  
698 Dune Field. In: *Lunar and Planetary Institute Science Conference Abstracts*. Vol. 32 of *Lunar and  
699 Planetary Inst. Technical Report*. pp. 1966–+.
- 700 Toon, O. B., McKay, C. P., Ackerman, T. P., Santhanam, K., 1989. Rapid calculation of radiative heating  
701 rates and photodissociation rates in inhomogeneous multiple scattering atmospheres. *J. Geophys. Res.*  
702 94, 16,287–16,301.
- 703 Vincendon, M., Langevin, Y., 2010. A spherical Monte-Carlo model of aerosols: Validation and first  
704 applications to Mars and Titan. *Icarus* 207, 923–931.
- 705 Vincendon, M., Langevin, Y., Douté, S., Bibring, J., 2009. 3 Mars Years of Dust Optical Depth Mapping  
706 by OMEGA Above the South Pole. *LPI Contributions* 1494, 59–60.
- 707 Vincendon, M., Langevin, Y., Poulet, F., Bibring, J.-P., Gondet, B., 2007. Recovery of surface reflectance  
708 spectra and evaluation of the optical depth of aerosols in the near-IR using a Monte Carlo approach:  
709 Application to the OMEGA observations of high-latitude regions of Mars. *J. Geophys. Res.* 112 (E11),  
710 8–+.
- 711 Vincendon, M., Langevin, Y., Poulet, F., Bibring, J.-P., Gondet, B., Jouglet, D., OMEGA Team, 2008.  
712 Dust aerosols above the south polar cap of Mars as seen by OMEGA. *Icarus* 196, 488–505.
- 713 Warren, S. G., 1986. Optical constants of carbon dioxide ice. *Appl. Opt.* 25, 2650–2674.
- 714 Warren, S. G., Wiscombe, W. J., Firestone, J. F., 1990. Spectral albedo and emissivity of CO<sub>2</sub> in Martian  
715 polar caps: model results. *J. Geophys. Res.* 95, 717–741.
- 716 Williams, K. E., Toon, O. B., Heldmann, J. L., McKay, C., Mellon, M. T., 2008. Stability of mid-latitude

717 snowpacks on Mars. *Icarus* 196, 565–577.

718 Wolf, M. J., Smith, M. D., Clancy, R. T., Arvidson, R., Kahre, M., Seelos, F., Murchie, S., Savijärvi,  
719 H., 2009. Wavelength dependence of dust aerosol single scattering albedo as observed by the Compact  
720 Reconnaissance Imaging Spectrometer. *Journal of Geophysical Research (Planets)* 114, 0–+.

ACCEPTED MANUSCRIPT

## 721 List of Figures

722	1	Energy terms used in our model (solar flux (0.1-5 $\mu\text{m}$ ), incident thermal flux, thermal emission, sensible heat flux, geothermal heat flux, and latent heat flux when there is a phase transition). . . . .	33
723			
724			
725	2	Evolution of the solar zenith angle at 85° S latitude. Dotted line represents the maximum angle and the dashed line the minimum angle. At this latitude, the end of the polar night occurs around Ls 168°. The sun remains close to the horizon during spring. . . . .	34
726			
727			
728			
729	3	Evolution of the Fresnel reflection coefficient of a flat CO <sub>2</sub> ice layer with solar incidence angle, as defined by Eq. 11, 12 and 13. The reflection coefficient increases very quickly after 60°, a typical case for the polar regions. Fresnel reflection can therefore severely limit solar radiation penetration in these areas. . . . .	35
730			
731			
732			
733			
734	4	Fraction of the solar flux ("I/F") reaching the surface as a function of the solar zenith angle (I/F = 1 for a sun at zenith without atmosphere). The direct and scattered components of the solar flux reaching the surface are detailed (red and green curves respectively - total in black). For solar zenith angles greater than 85° more than half of the solar flux reaching the surface is due to aerosol scattering. After the terminator (no more direct component), aerosols still significantly illuminate the surface for a few degrees. Solid lines are results obtained through the use of the model and Mars dust parameters detailed in Vincendon et Langevin (2010), while the dashed lines represent the analytical model used in this study. . . . .	36
735			
736			
737			
738			
739			
740			
741			
742			
743			
744	5	Evolution of the interaction between the CO <sub>2</sub> ice layer and the solar flux as a function of CO <sub>2</sub> grain radius in meters (CO <sub>2</sub> snow model). Ice thickness=0.6 m; incident solar angle=60°; ground albedo=0.24; no dust content. As the effective grain radius increases, the reflected part decreases and the part absorbed in the ice increases. However, photons are not yet able to reach the regolith until the effective radius is higher than about 1 $\mu\text{m}$ . As the effective radius continues to increase, photons can go through the ice more easily and the part absorbed in the ice begins to decrease. . . . .	37
745			
746			
747			
748			
749			
750			
751			
752	6	Evolution of the interaction between the CO <sub>2</sub> ice layer and the solar flux as a function of dust content (slab model). Ice thickness=0.6 m; incident solar angle=60°; ground albedo=0.24. As the dust contamination increases, it becomes much more difficult for photons to penetrate into the ice. With a dust contamination of 10 ppm, less than 40 % of solar radiation is absorbed by the regolith and with 100 ppm, it decreases to less than 1 %. . . . .	38
753			
754			
755			
756			
757			
758	7	Sublimation temperature in a CO <sub>2</sub> ice slab for surface pressure equal to 507 Pa. Material is an homogeneous CO <sub>2</sub> ice slab with a density of 1606 kg m <sup>-3</sup> . . . . .	39
759			
760			
761	8	Temperature profile at different Ls for clean CO <sub>2</sub> ice on a flat terrain (local time: 12AM) at 85° S (late winter / early spring). Solid lines are simulations with a clean slab, dashed lines are simulations with a slab contaminated by 10 ppm of dust. Temperature at the regolith interface increases after the end of the polar night and basal sublimation begins at Ls 191°. . . . .	40
762			
763			
764			
765			
766			



- 767 9 Continuation of Fig. 8 (mid-spring to fall equinox). The x-axis limits  
768 have been changed to 145-300K for clarity. CO<sub>2</sub> ice disappears at about  
769 Ls 240°. Then the surface quickly heats and reaches 260 K after a few  
770 martian days. During fall, surface temperature decreases down to the  
771 condensation temperature and CO<sub>2</sub> ice begins to accumulate. . . . . 41
- 772 10 Same as Fig. 8 but for a 30° north oriented slope (equator-facing). Tem-  
773 perature at the regolith interface increases much faster than for a flat  
774 terrain after the end of the polar night and basal sublimation begins at Ls  
775 174°. . . . . 42
- 776 11 Continuation of Fig. 10 (mid-spring to fall equinox). CO<sub>2</sub> ice disappears  
777 at about Ls 220°. Then the surface temperature quickly heats up and  
778 reaches 260 K after a few martian days and 290 K after about 50 martian  
779 days. . . . . 43
- 780 12 Different behaviors of the CO<sub>2</sub> ice depending on effective grain size and  
781 dust content. Zone 1 represents the zone where both surface and basal  
782 sublimation occur ; zone 2, is the same as zone 1 but here sublimation  
783 temperature is reached within the ice before being reached at the base ;  
784 zone 3, the zone where only surface sublimation occurs ; zone 4 the zone  
785 where CO<sub>2</sub> ice accumulates year after year. Simulations were run on a flat  
786 terrain at 85° S. . . . . 44
- 787 13 Same as Fig. 8 but for small-grained CO<sub>2</sub> ice (effective radius: 130 μm,  
788 200 ppm of dust). As the photons are not able to penetrate into the CO<sub>2</sub>  
789 ice, temperature within the ice stays close to 145 K. In this case, the albedo  
790 is higher than for slab ice and CO<sub>2</sub> ice does not disappear until about Ls  
791 295°. . . . . 45
- 792 14 Same as Fig. 8 but for CO<sub>2</sub> ice with an effective grain radius of 2.5 cm  
793 and a dust contamination of 10 ppm. Sublimation temperature is reached  
794 within the ice at about Ls 218°. We limit the covered period here, since  
795 we think that gas bubbles will form around and ice will crack. CO<sub>2</sub> ice  
796 properties and involved processes will therefore change after that point. . . 46
- 797 15 Evolution of the difference between the sublimation temperature and the  
798 temperature within the CO<sub>2</sub> ice (same parameters as in Fig. 14). Subli-  
799 mation temperature is reached at about 9 cm depth. . . . . 47
- 800 16 Temperature profile at local 12AM (blue) and 12PM (orange) for a clean  
801 CO<sub>2</sub> ice slab on a flat terrain at 85° S. Energy storage in the slab is  
802 apparent. Furthermore, the largest temperature difference between 12AM  
803 and 12PM occurs at the regolith interface. Once CO<sub>2</sub> ice has disappeared,  
804 there are daily thermal waves. . . . . 48

- 805 17 Evolution of the amount of CO<sub>2</sub> ice for small-grained dusty (100 ppm) CO<sub>2</sub>  
806 ice (left) and a clean slab (right) at 85° S. Considering the plot on the left  
807 and the left part of this plot (before reaching the maximum), we can see  
808 that CO<sub>2</sub> ice condenses at night (the CO<sub>2</sub> ice amount increases) and CO<sub>2</sub>  
809 ice sublimates during the day (the CO<sub>2</sub> ice amount decreases). However,  
810 in the case of translucent CO<sub>2</sub> ice, the amount of CO<sub>2</sub> ice never decreases  
811 before reaching the maximum. This is due to the fact that the solar flux  
812 penetrates in the case of a translucent slab and does not appreciably slow  
813 the condensation process whereas this same flux sublimates the ice in the  
814 case of small grains with little penetration. After the end of the polar  
815 night, in the case of slab ice, energy storage makes condensation during  
816 the night very difficult to achieve. . . . . 49
- 817 18 Evolution of the solar longitude L<sub>s</sub> (deg) of the first gas ejection with  
818 slope and orientation (left) and evolution of CO<sub>2</sub> ice maximum amount  
819 (kg m<sup>-2</sup>) (right) at 85° S (slab model is used). Both are directly linked to  
820 the insolation and therefore present similar patterns. We can notice that  
821 basal sublimation can occur on pole-facing slopes. . . . . 50
- 822 19 Evolution of the solar longitude L<sub>s</sub> (deg) of the first gas ejection with  
823 respect to the regolith thermal inertia at 85° S (slab model). Contrary  
824 to what was expected, increasing the regolith thermal inertia does not  
825 accelerate the beginning of the venting process but delays it (less than  
826 10° of L<sub>s</sub> in the considered range). . . . . 51
- 827 20 Evolution of the solar longitude L<sub>s</sub> (deg) of the first gas ejection with  
828 respect to the regolith albedo at 85° S for a flat terrain (crosses) and for  
829 a 30° north oriented slope (triangles). Slab model is used. Since the slab  
830 is translucent, a large part of the energy reaches the regolith. Therefore,  
831 when we decrease the albedo, the fraction of the solar flux that penetrates  
832 into the regolith does not increase enough to accelerate significantly the  
833 beginning of the venting process. . . . . 52
- 834 21 Evolution of the solar longitude L<sub>s</sub> (deg) of the first gas ejection and of CO<sub>2</sub>  
835 ice maximum amount with respect to the latitude (slab model). Surface  
836 pressure was set to 400 Pa in the southern hemisphere and to 1000 Pa in  
837 the northern hemisphere. Results show that the venting process can also  
838 occur in the northern hemisphere. . . . . 53
- 839 22 MOC image of a dune field at 62° S and L<sub>s</sub> 174°. Dark spots seem to be  
840 present only on dunes. . . . . 54
- 841 23 HiRISE image of a dune field at 80° N and L<sub>s</sub> 105°. We can notice the  
842 albedo difference between dune material and the surroundings, since the  
843 seasonal CO<sub>2</sub> ice cap has disappeared. . . . . 55
- 844 24 HiRISE image of the same dune field as on Fig. 23, but at different L<sub>s</sub>.  
845 Dark spots are clearly visible on dunes (blue circle). Some gray patterns  
846 are also visible around at L<sub>s</sub> 20° and possibly at L<sub>s</sub> 70° (red circles) in the  
847 surrounding terrain. . . . . 56

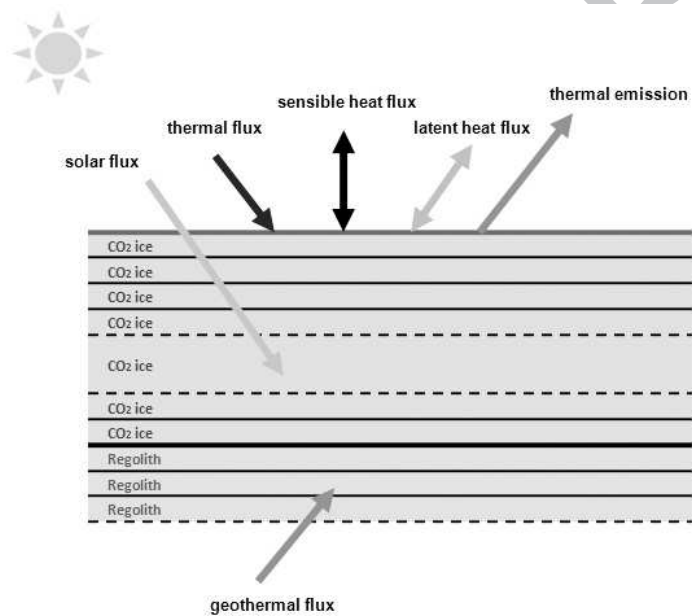


Figure 1: Energy terms used in our model (solar flux ( $0.1-5 \mu\text{m}$ ), incident thermal flux, thermal emission, sensible heat flux, geothermal heat flux, and latent heat flux when there is a phase transition).

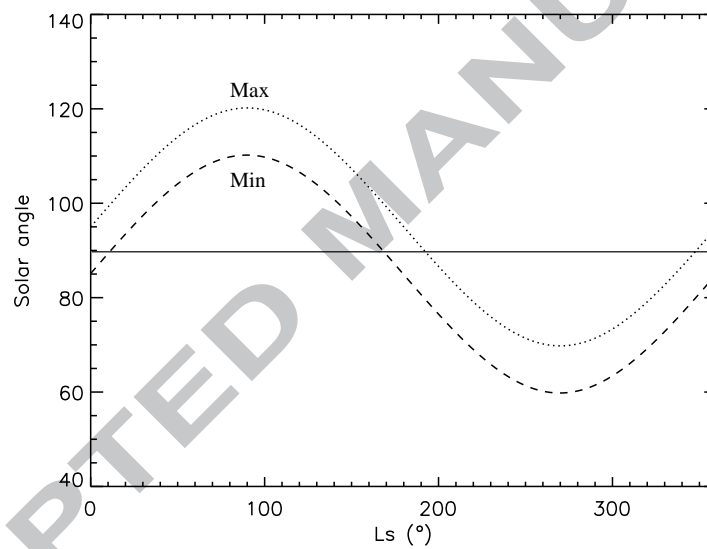


Figure 2: Evolution of the solar zenith angle at  $85^{\circ}$  S latitude. Dotted line represents the maximum angle and the dashed line the minimum angle. At this latitude, the end of the polar night occurs around  $Ls 168^{\circ}$ . The sun remains close to the horizon during spring.

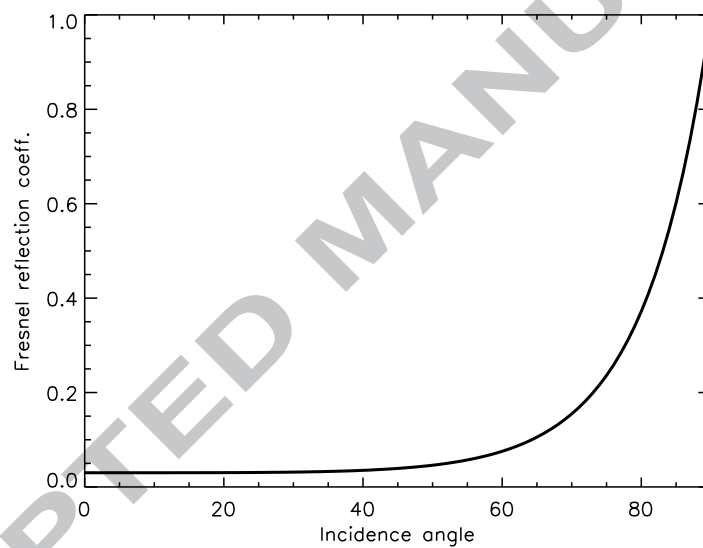


Figure 3: Evolution of the Fresnel reflection coefficient of a flat CO<sub>2</sub> ice layer with solar incidence angle, as defined by Eq. 11, 12 and 13. The reflection coefficient increases very quickly after 60°, a typical case for the polar regions. Fresnel reflection can therefore severely limit solar radiation penetration in these areas.

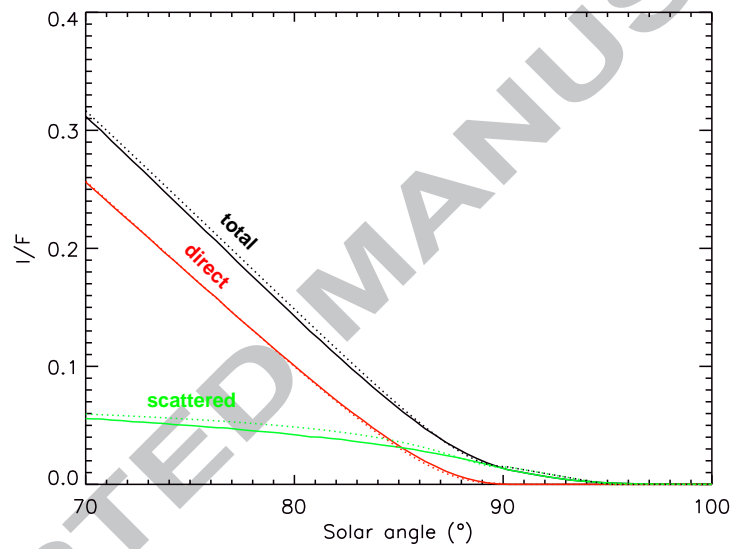


Figure 4: Fraction of the solar flux ( $I/F$ ) reaching the surface as a function of the solar zenith angle ( $I/F = 1$  for a sun at zenith without atmosphere). The direct and scattered components of the solar flux reaching the surface are detailed (red and green curves respectively - total in black). For solar zenith angles greater than 85 more than half of the solar flux reaching the surface is due to aerosol scattering. After the terminator (no more direct component), aerosols still significantly illuminate the surface for a few degrees. Solid lines are results obtained through the use of the model and Mars dust parameters detailed in Vincendon et Langevin (2010), while the dashed lines represent the analytical model used in this study.

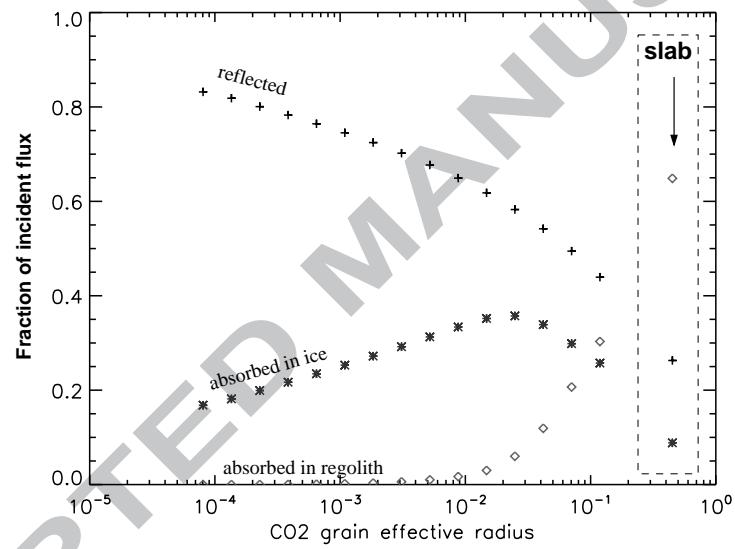


Figure 5: Evolution of the interaction between the CO<sub>2</sub> ice layer and the solar flux as a function of CO<sub>2</sub> grain radius in meters (CO<sub>2</sub> snow model). Ice thickness=0.6 m; incident solar angle=60°; ground albedo=0.24; no dust content. As the effective grain radius increases, the reflected part decreases and the part absorbed in the ice increases. However, photons are not yet able to reach the regolith until the effective radius is higher than about 1 mm. As the effective radius continues to increase, photons can go through the ice more easily and the part absorbed in the ice begins to decrease.

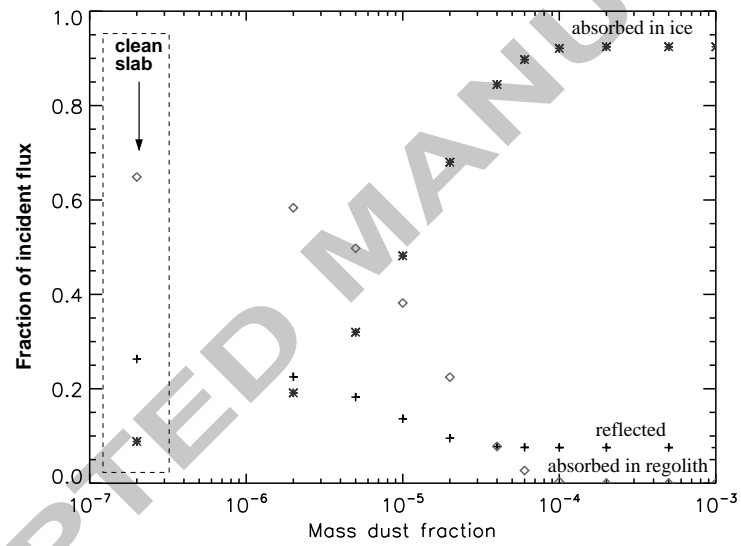


Figure 6: Evolution of the interaction between the CO<sub>2</sub> ice layer and the solar flux as a function of dust content (slab model). Ice thickness=0.6 m; incident solar angle=60°; ground albedo=0.24. As the dust contamination increases, it becomes much more difficult for photons to penetrate into the ice. With a dust contamination of 10 ppm, less than 40 % of solar radiation is absorbed by the regolith and with 100 ppm, it decreases to less than 1 %.



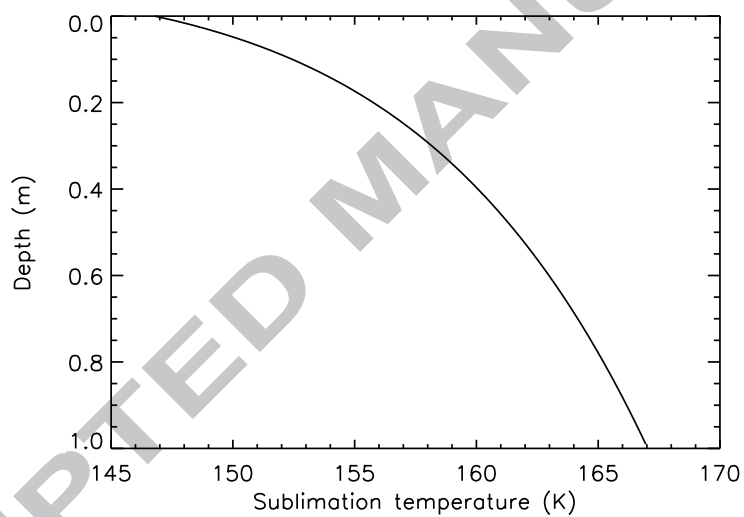


Figure 7: Sublimation temperature in a CO<sub>2</sub> ice slab for surface pressure equal to 507 Pa. Material is an homogeneous CO<sub>2</sub> ice slab with a density of 1606 kg m<sup>-3</sup>.

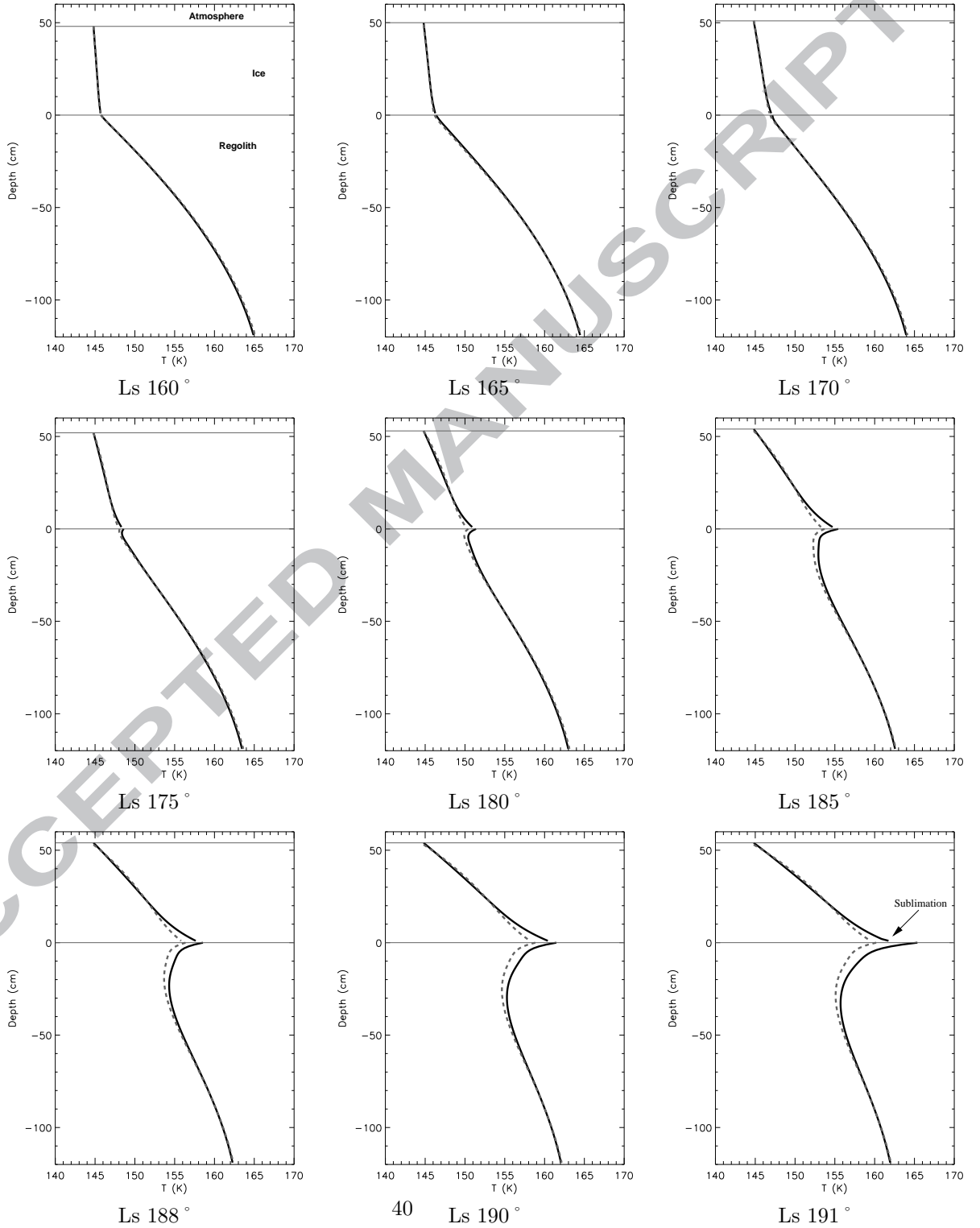


Figure 8: Temperature profile at different Ls for clean CO<sub>2</sub> ice on a flat terrain (local time: 12AM) at 85° S (late winter / early spring). Solid lines are simulations with a clean slab, dashed lines are simulations with a slab contaminated by 10 ppm of dust. Temperature at the regolith interface increases after the end of the polar night and basal sublimation begins at Ls 191°.

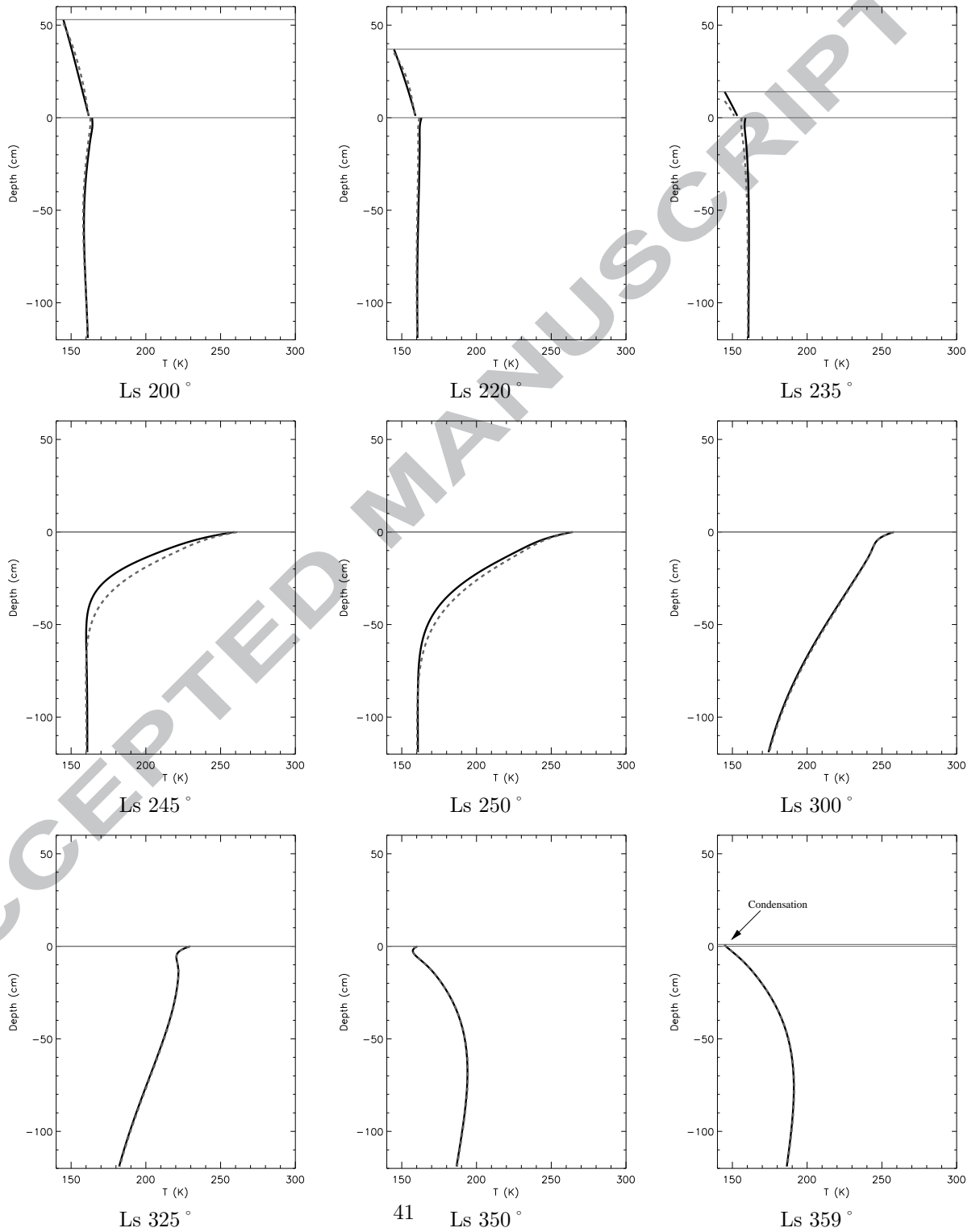


Figure 9: Continuation of Fig. 8 (mid-spring to fall equinox). The x-axis limits have been changed to 145-300K for clarity. CO<sub>2</sub> ice disappears at about Ls 240°. Then the surface quickly heats and reaches 260 K after a few martian days. During fall, surface temperature decreases down to the condensation temperature and CO<sub>2</sub> ice begins to accumulate.

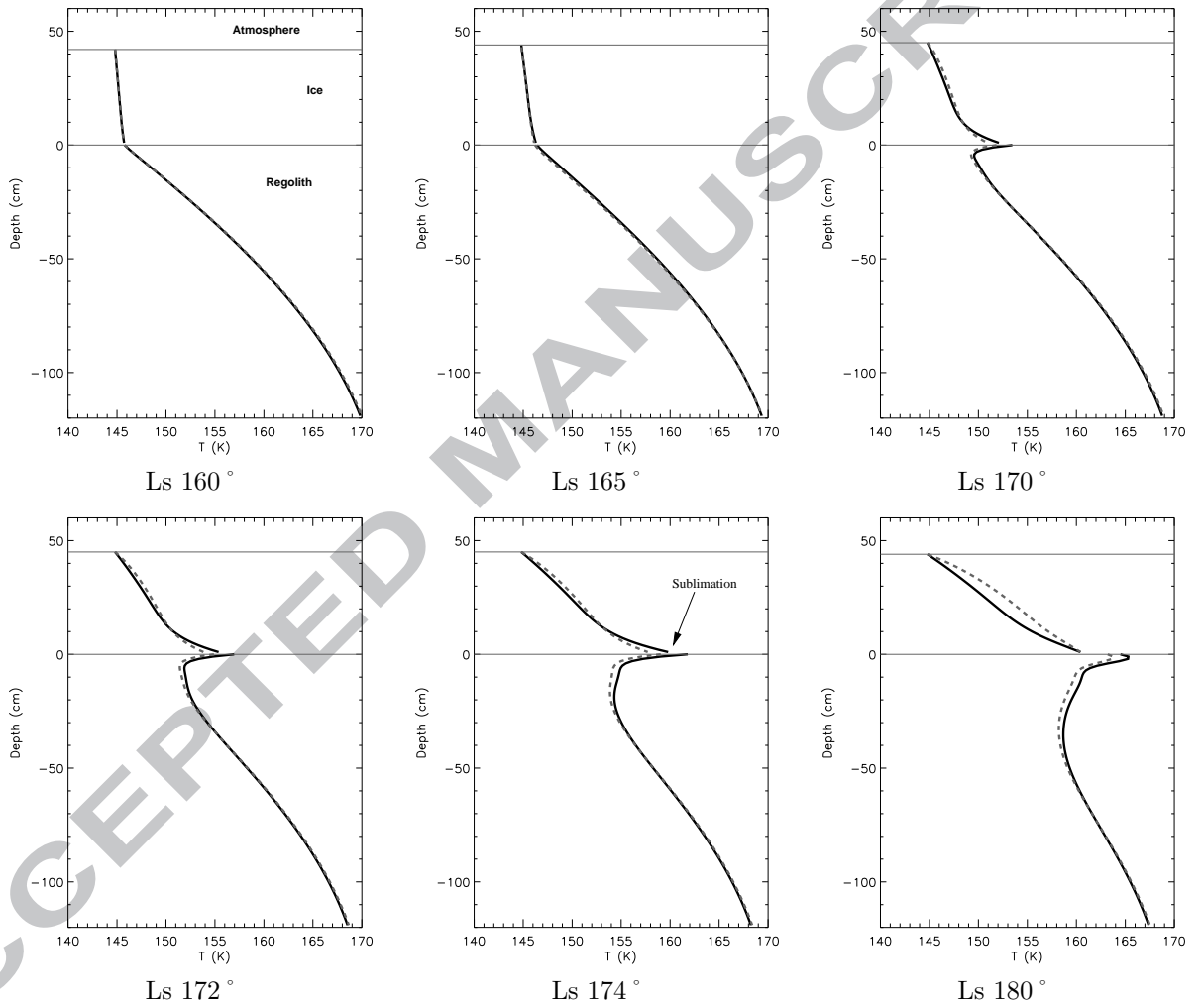


Figure 10: Same as Fig. 8 but for a 30° north oriented slope (equator-facing). Temperature at the regolith interface increases much faster than for a flat terrain after the end of the polar night and basal sublimation begins at Ls 174°.

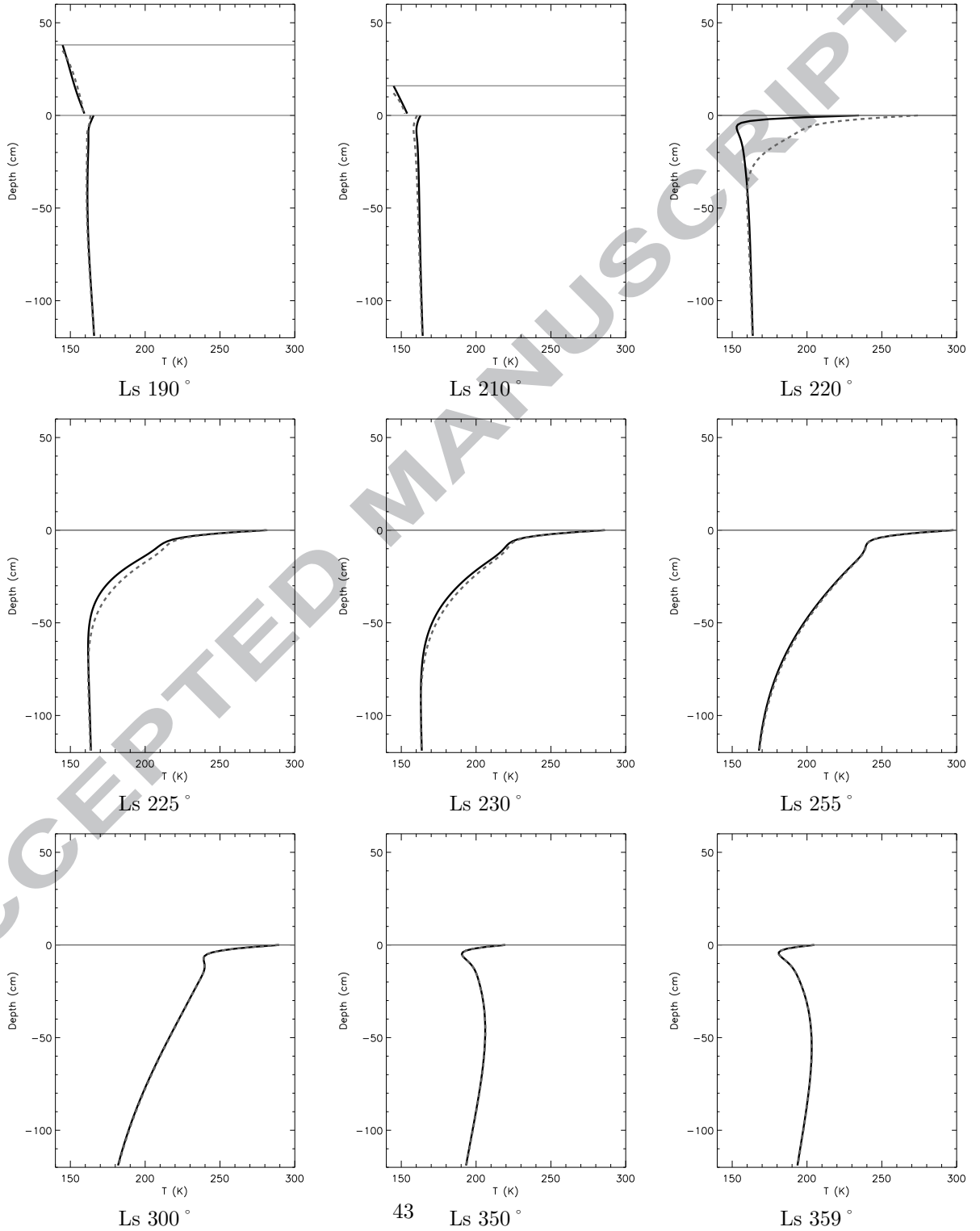


Figure 11: Continuation of Fig. 10 (mid-spring to fall equinox). CO<sub>2</sub> ice disappears at about Ls 220°. Then the surface temperature quickly heats up and reaches 260 K after a few martian days and 290 K after about 50 martian days.

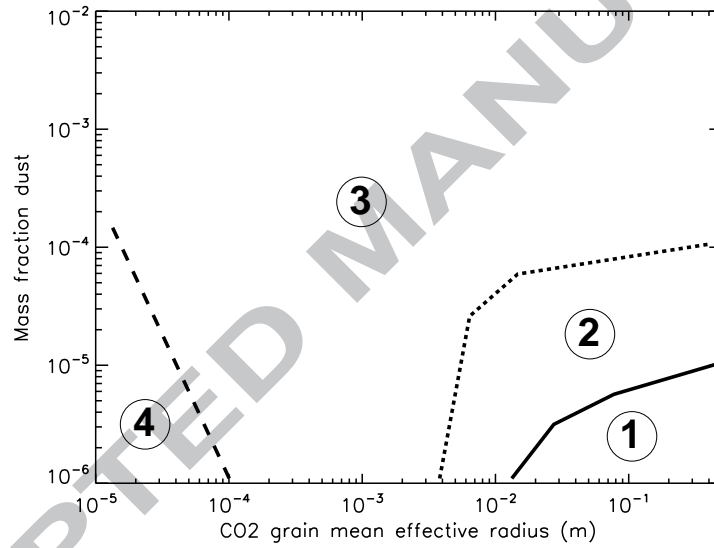


Figure 12: Different behaviors of the CO<sub>2</sub> ice depending on effective grain size and dust content. Zone 1 represents the zone where both surface and basal sublimation occur ; zone 2, is the same as zone 1 but here sublimation temperature is reached within the ice before being reached at the base ; zone 3, the zone where only surface sublimation occurs ; zone 4 the zone where CO<sub>2</sub> ice accumulates year after year. Simulations were run on a flat terrain at 85 °S.

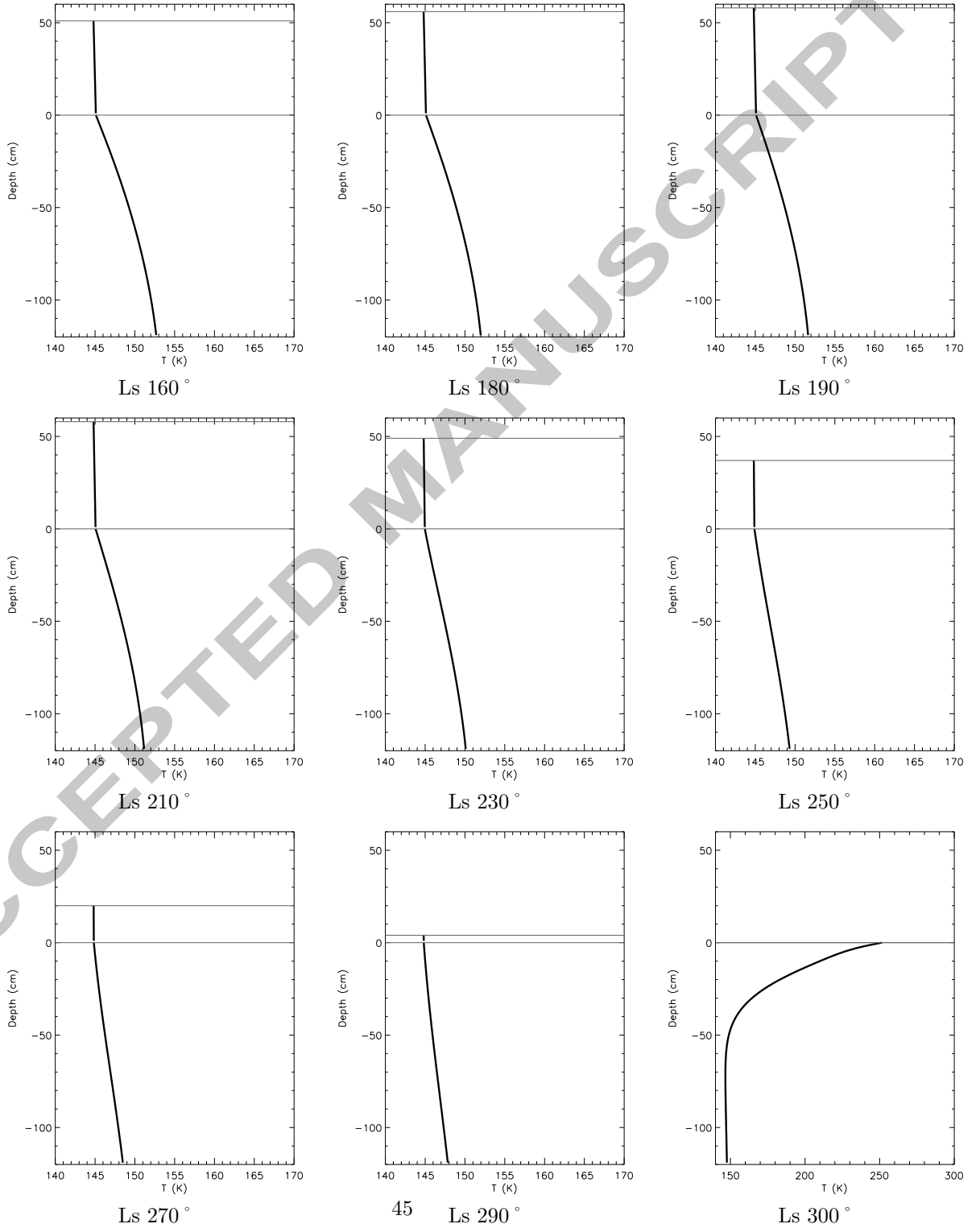


Figure 13: Same as Fig. 8 but for small-grained CO<sub>2</sub> ice (effective radius: 130  $\mu\text{m}$ , 200 ppm of dust). As the photons are not able to penetrate into the CO<sub>2</sub> ice, temperature within the ice stays close to 145 K. In this case, the albedo is higher than for slab ice and CO<sub>2</sub> ice does not disappear until about Ls 295°.

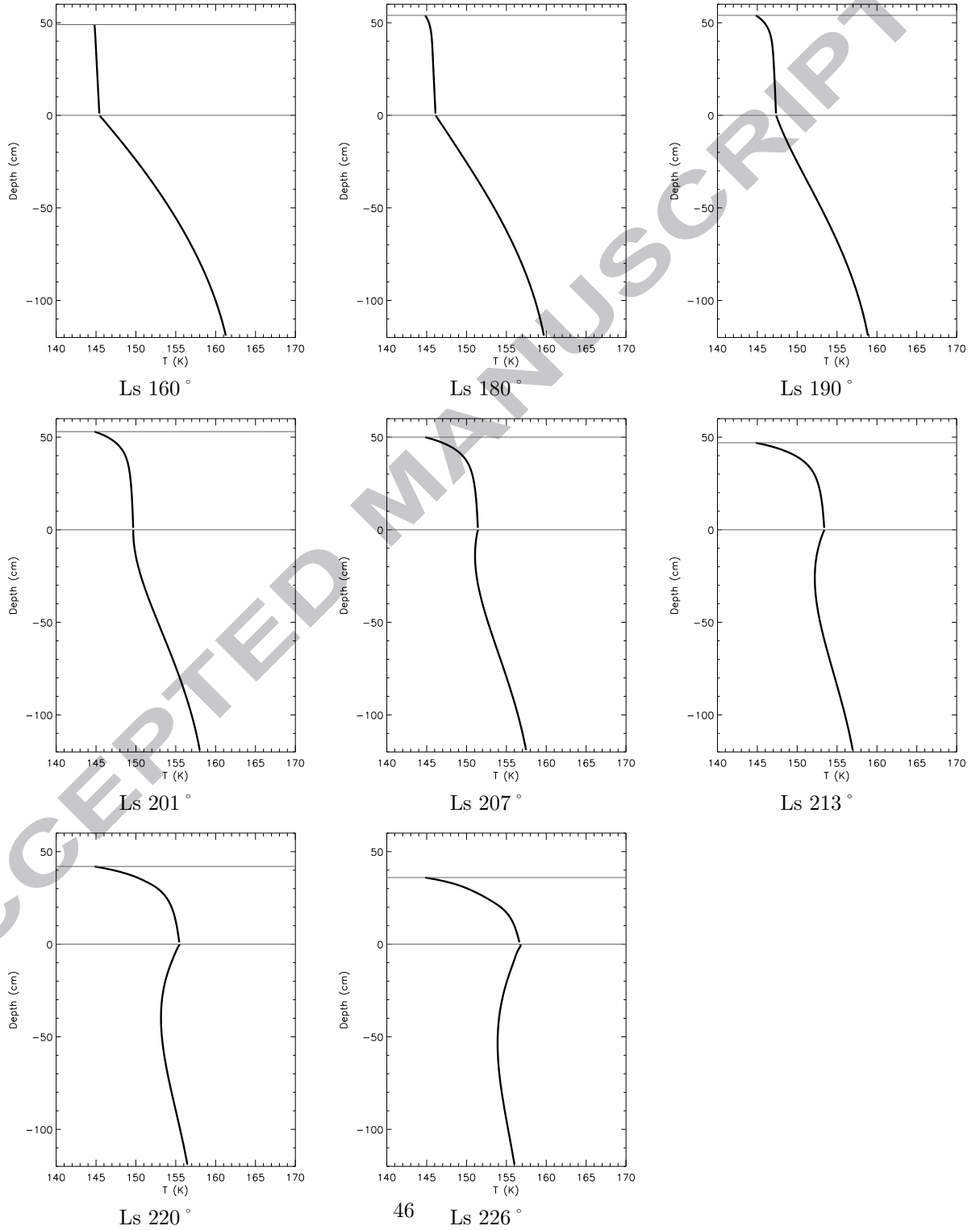


Figure 14: Same as Fig. 8 but for CO<sub>2</sub> ice with an effective grain radius of 2.5 cm and a dust contamination of 10 ppm. Sublimation temperature is reached within the ice at about Ls 218°. We limit the covered period here, since we think that gas bubbles will form around and ice will crack. CO<sub>2</sub> ice properties and involved processes will therefore change after that point.



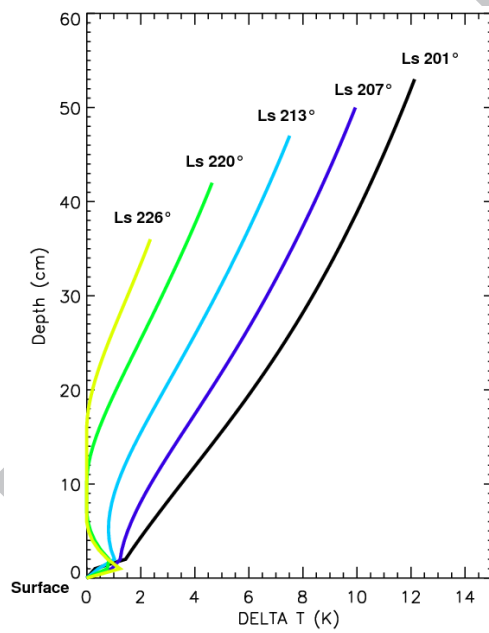


Figure 15: Evolution of the difference between the sublimation temperature and the temperature within the CO<sub>2</sub> ice (same parameters as in Fig. 14). Sublimation temperature is reached at about 9 cm depth.

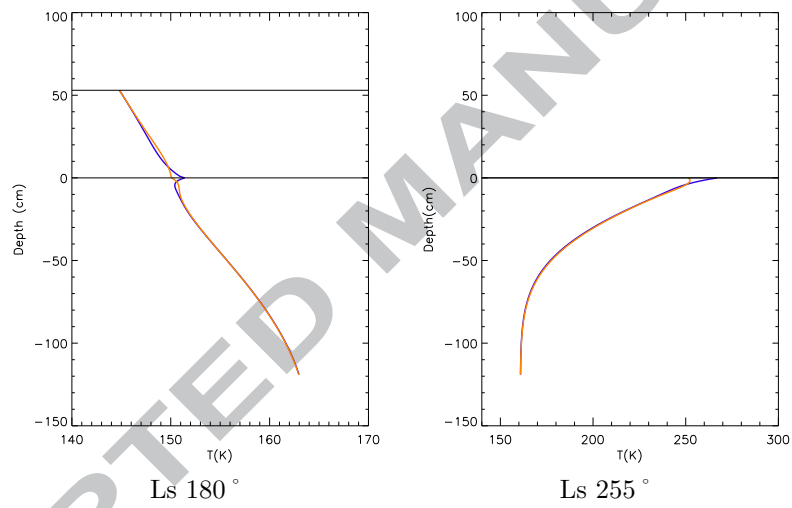


Figure 16: Temperature profile at local 12AM (blue) and 12PM (orange) for a clean CO<sub>2</sub> ice slab on a flat terrain at 85° S. Energy storage in the slab is apparent. Furthermore, the largest temperature difference between 12AM and 12PM occurs at the regolith interface. Once CO<sub>2</sub> ice has disappeared, there are daily thermal waves.

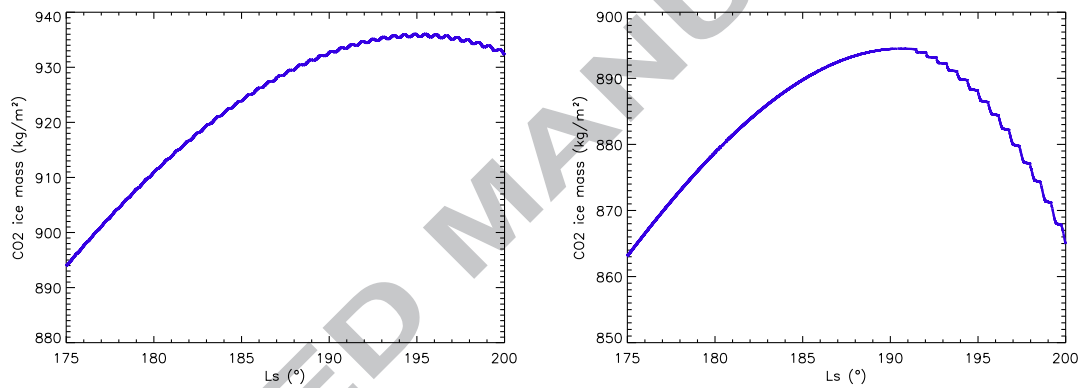


Figure 17: Evolution of the amount of CO<sub>2</sub> ice for small-grained dusty (100 ppm) CO<sub>2</sub> ice (left) and a clean slab (right) at 85° S. Considering the plot on the left and the left part of this plot (before reaching the maximum), we can see that CO<sub>2</sub> ice condenses at night (the CO<sub>2</sub> ice amount increases) and CO<sub>2</sub> ice sublimates during the day (the CO<sub>2</sub> ice amount decreases). However, in the case of translucent CO<sub>2</sub> ice, the amount of CO<sub>2</sub> ice never decreases before reaching the maximum. This is due to the fact that the solar flux penetrates in the case of a translucent slab and does not appreciably slow the condensation process whereas this same flux sublimates the ice in the case of small grains with little penetration. After the end of the polar night, in the case of slab ice, energy storage makes condensation during the night very difficult to achieve.

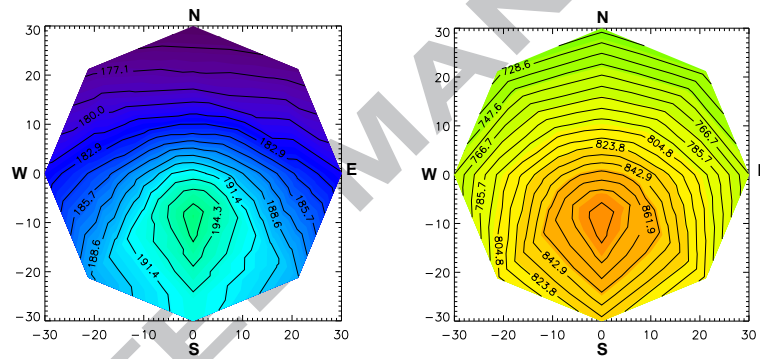


Figure 18: Evolution of the solar longitude  $L_s$  (deg) of the first gas ejection with slope and orientation (left) and evolution of  $\text{CO}_2$  ice maximum amount ( $\text{kg m}^{-2}$ ) (right) at  $85^\circ \text{S}$  (slab model is used). Both are directly linked to the insolation and therefore present similar patterns. We can notice that basal sublimation can occur on pole-facing slopes.

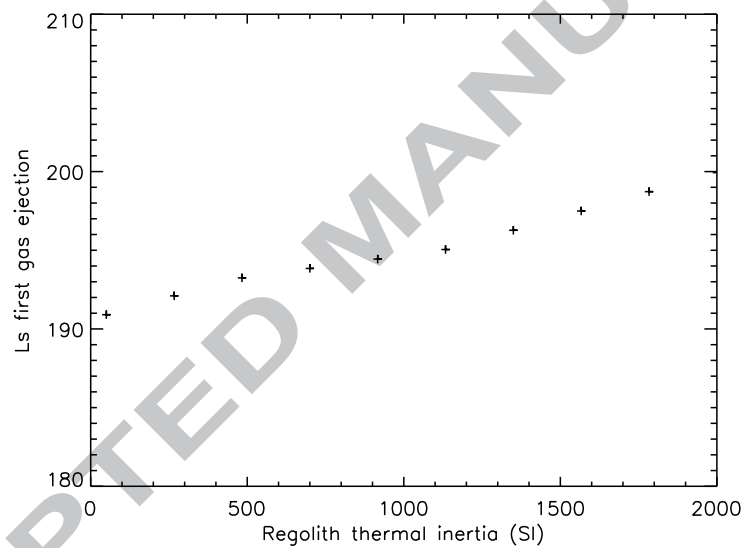


Figure 19: Evolution of the solar longitude  $L_s$  (deg) of the first gas ejection with respect to the regolith thermal inertia at  $85^\circ$  S (slab model). Contrary to what was expected, increasing the regolith thermal inertia does not accelerate the beginning of the venting process but delays it (less than  $10^\circ$  of  $L_s$  in the considered range).

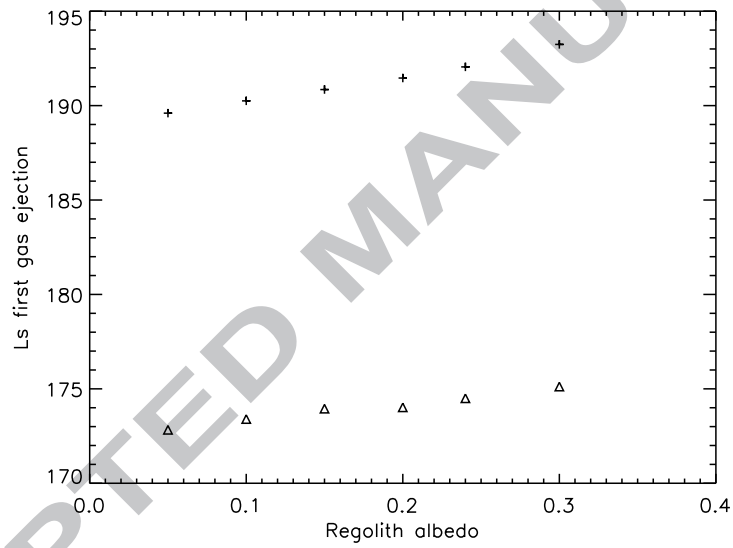


Figure 20: Evolution of the solar longitude  $L_s$  (deg) of the first gas ejection with respect to the regolith albedo at  $85^\circ$  S for a flat terrain (crosses) and for a  $30^\circ$  north oriented slope (triangles). Slab model is used. Since the slab is translucent, a large part of the energy reaches the regolith. Therefore, when we decrease the albedo, the fraction of the solar flux that penetrates into the regolith does not increase enough to accelerate significantly the beginning of the venting process.

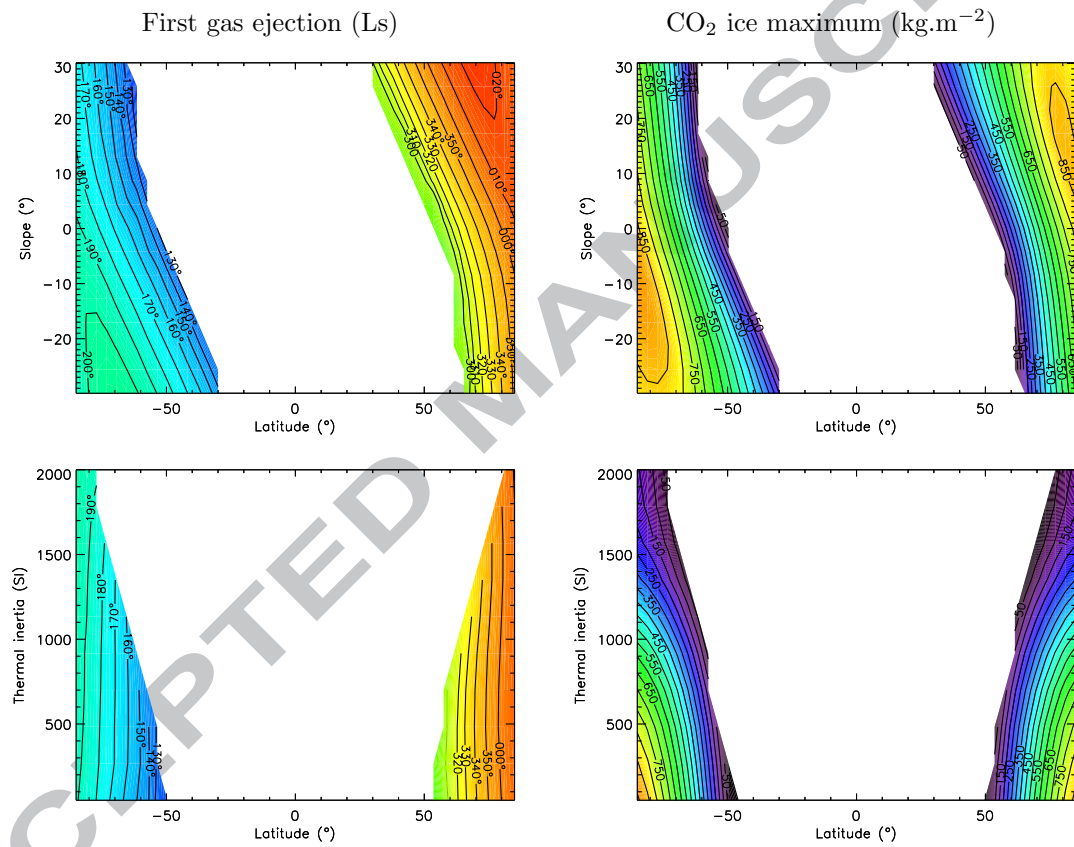


Figure 21: Evolution of the solar longitude  $L_s$  (deg) of the first gas ejection and of CO<sub>2</sub> ice maximum amount with respect to the latitude (slab model). Surface pressure was set to 400 Pa in the southern hemisphere and to 1000 Pa in the northern hemisphere. Results show that the venting process can also occur in the northern hemisphere.

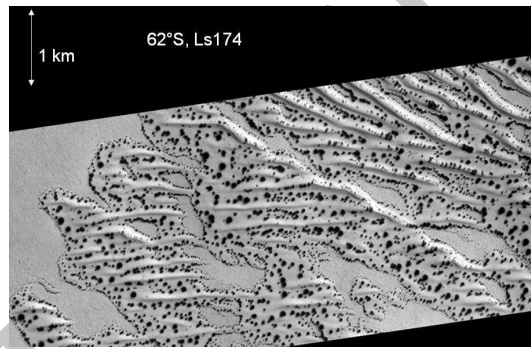


Figure 22: MOC image of a dune field at  $62^{\circ}$  S and Ls  $174^{\circ}$ . Dark spots seem to be present only on dunes.



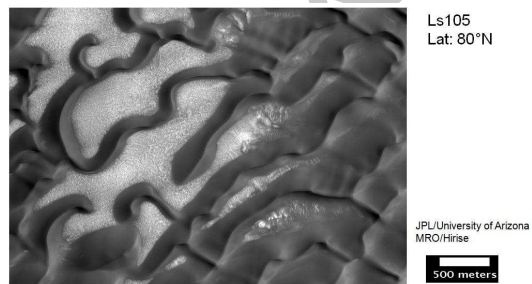


Figure 23: HiRISE image of a dune field at  $80^{\circ}\text{N}$  and  $Ls\ 105^{\circ}$ . We can notice the albedo difference between dune material and the surroundings, since the seasonal  $\text{CO}_2$  ice cap has disappeared.

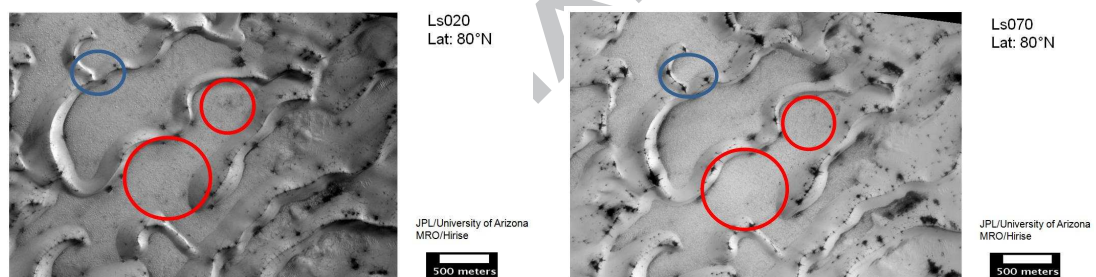


Figure 24: HiRISE image of the same dune field as on Fig. 23, but at different Ls. Dark spots are clearly visible on dunes (blue circle). Some gray patterns are also visible around at Ls 20° and possibly at Ls 70° (red circles) in the surrounding terrain.

## Research highlights:

- CO<sub>2</sub> ice basal sublimation is possible under certain conditions on Mars.
- Different CO<sub>2</sub> ice properties lead to different sublimation processes.
- Solar radiation alone can initiate basal sublimation in polar regions.

ACCEPTED MANUSCRIPT